UC San Diego
UC San Diego Electronic Theses and Dissertations

Title

Silicon-rich Nitride as a versatile and highly non-linear CMOS compatible material platform.

Permalink
https://escholarship.org/uc/item/1hv0d2wq

Author
Friedman, Alex Michael

Publication Date
2022

Peer reviewed|Thesis/dissertation

eScholarship.org
Powered by the California Digital Library
University of California

UNIVERSITY OF CALIFORNIA SAN DIEGO

Silicon-rich Nitride as a versatile and highly non-linear CMOS compatible material platform.

A Dissertation submitted in partial satisfaction of the requirements
for the degree Doctor of Philosophy

in

Electrical Engineering (Photonics)

by

Alex Friedman

Committee in charge:

Professor Yeshaiahu Fainman, chair
Professor Andrew Kummel
Professor Vitaliy Lomakin
Professor Paul Yu

2022

Copyright

Alex Friedman, 2022

All rights reserved.

The Dissertation of Alex Friedman is approved, and it is acceptable in quality and form for publication on microfilm and electronically.

University of California San Diego

2022

DEDICATION

I dedicate my thesis to my parents and siblings, the love and support of whom, near or far, was crucial throughout my education. One chapter now ends, but great things to those who show dedication and hard work, so on to the next!

We lie best when we lie to ourselves.

-Stephen King, It

TABLE OF CONTENTS

DISSERTATION APPROVAL PAGE iii

DEDICATION iv

TABLE OF CONTENTS v

LIST OF FIGURES vi

LIST OF TABLES viii

ACKNOWLEDGEMENTS ix

VITA xi

ABSTRACT OF THE DISSERTATION xii

INTRODUCTION 1

CHAPTER 1 – THE DC-KERR EFFECT IN SILICON-RICH NITRIDE 4

CHAPTER 2 – OPTICAL BISTABILITY IN PECVD SILICON-RICH NITRIDE 21

CHAPTER 3 - A SYSTEMATIC EVALUATION OF SILICON-RICH NITRIDE ELECTRO-OPTIC MODULATOR DESIGN AND TRADEOFFS 35

REFERENCES 56

LIST OF FIGURES

Figure 1: (a) Optical microscope image of our point coupled ring resonator with electrode width and spacing marked with white arrows and text overlay. (b) Scanning Electron Microscope image of the point coupler region of a racetrack ring resonator with the FOX-16 on top of the post etched waveguides.. 8

Figure 2: Above the top cladding there are electrodes 220 μm in length on each of the two straight arm sections. All measured data is operated in the TM polarization for a 320 nm thick 450 nm wide SRN waveguide. (a) Measurement of the transmission versus wavelength along with the best fit 11

Figure 3: (a) Schematic breakdown of the test structure used to extract the RF permittivity. Capacitance vs voltage measurements are performed using an Agilent B1500A semiconductor device analyzer. Thickness 'd' = 150nm. (b) Capacitance [pF] vs Voltage [V] at 100 kHz 15

Figure 4: Current [A] vs voltage [V] up to the point of breakage plotted on a semilog scale both pre- and post- anneal at 300°C. As can be seen, annealing of these films does improve the maximum safe electric field strength with post annealing is 1.2 x 10^8 [V/m] as opposed to 8.3 x 10^7 [V/m] pre-annealing. 16

Figure 5: A plot of Linear refractive index at a wavelength of 800nm using ellipsometry as a function of annealing temperature. All films where deposited at the same time at 350°C. These films were then individually annealed for 15 mins in a forming gas ambient at the listed temperature 17

Figure 6: (a) A schematic breakdown of the phase shifter design shown as a cut out. The goal of this design is to have the applied field distribution to be as uniform and directional as possible. The electrode traces are 30μm wide electrode and separated by 10 μm. These electrodes are patterned using liftoff from 18

Figure 7: In isotropic media the above tensor components are the 21 non-zero elements. The subscripts 1, 2, and 3 represent the three-principle axis 'i', 'j', and 'k'. From our design of the electrodes we can conclude that any terms with mixed contributions from the applied field, labeled as 'Edc'. 19

Figure 8: Optical microscope image of the PECVD SRN 45um bend radius all-pass ring resonator device. 24

Figure 9: Normalized transmission spectra at low input power for the SRN ring device operating in the TM-like mode. Shown is a fitting for the transmission spectra's line shape we determine the propagation loss to be 3.38dB/cm for a group index of 3.522 ± 0.156. 25

Figure 10: (a) Transmission spectra of a 45um SRN ring resonator for the corresponding on-chip powers in (b). Notice how at the lowest laser power presented the asymmetry is

reduced and as the laser power increases the resonant wavelength red-shifts and the resonance becomes increasingly asymmetric. ... 27

Figure 11: Transmission as a function of time for the ‘baseline’ curve as well as the ‘near resonance’ case for ramp ‘frequencies’ from 1kHz up to 150kHz. ... 29

Figure 12: (a) The transmission spectra of the ring resonator device at two different input powers, in black 3.98mW (6dBm), and in teal 10mW (10dBm). Notice how as the input power is increased the resonance becomes more asymmetric and the resonance point red shifts.. ... 31

Figure 13: (a) Normalized transmission as a function of time for a ‘0,1,0,1,0,1’ bit sequence. The two stable output states can be switched between using a control sequence on the input power that begins and ends at the same power level with a finite ΔPin differential of 0.4dB. ... 32

Figure 14: An example for a 10Ghz modulated Eac wave as a function of the fraction of Eac/Edc for a fixed Edc of 1.22×10^8 V/m. In the above plot the black dashed line represents the idealized case. ... 40

Figure 15: (a) Schematic cross-section of the proposed device structure. A Silicon-rich Nitride waveguide sits on a SiO_2 buried oxide layer. On top of the Silicon-rich Nitride waveguide is a thin dielectric shield layer onto which Ground-Signal-Ground gold electrodes are formed. Finally, the top of the structure is top clad with SiO_2. ... 43

Figure 16: (a) Effective Index of the TE-like and TM-like modes vs SiO_2 ‘shield’ thickness. (b) Overlap Integral of the TE-like and TM-like modes with the SRN waveguide core versus SiO_2 ‘shield’ thickness. (c) Effective Index of the TE-like and TM-like modes vs spacing from the electrode to waveguide sidewall. ... 43

Figure 17: (a) A plot of the change in refractive index under the presence of a combination of AC and DC field. In such a situation if we require that Edc >> Eac then we can write this as approximately $\Delta nac = \Delta nac\chi(2) + \Delta nac + dc\chi(3)$. (b) A plot of the require length for a π phase shift. ... 45

Figure 18: (a) Simulated Transmission spectra and maximum shift in transmission spectra for a 45um bend radius ring modulator assuming a $\Delta r - a = 0.05$ mismatch between the single pass amplitude transmission coefficient and the self-coupling coefficient of the bus ... 49

Figure 19: (a) Quality Factor versus electrode to sidewall spacing for shield thickness 100nm to 200nm (b) Photon lifetime limited bandwidth vs electrode to sidewall spacing for shield thickness 100nm to 200nm. ... 50

Figure 20: (a) Simulated Transmission spectra and maximum shift in transmission spectra for a MZI with an imbalance length of 200µm along with electrodes of the $L\pi$ length from section 3 in both arms driven in push-pull. (b) A plot of the $V\pi L\pi$ metric versus electrode to sidewall spacing and shield thickness ... 52

LIST OF TABLES

Table 1: A breakdown of the induced polarization..……………………………………………3

Table 2: Second and Third order contributions to the change in refractive index...…………3

Table 3: Example Possible Design parameters………………………………………………3

Table 4: A comparison of Modulator Performance …………………………………………3

ACKNOWLEDGEMENTS

I would like to acknowledge most importantly all of my family and friends, without whose support I certainly would never have made it this far. I would especially like to thank Jessica Medrado for the deep and passionate friendship during a difficult process and always pushing me to strive for more.

I express deep gratitude for to my advisor Professor Fairman, for taking me on as a graduate student, allowing me to pursue a variety of research of my own choosing, and providing guidance throughout the process. I would also like to express my gratitude towards all of the members of my committee for their guidance.

During my studies at the University of California San Diego I have met so many people and made so many friends during this process all of whom have made it very more enjoyable! Thank you to all of my colleagues at UCSD and especially, Hani Nejadriahi and Rajat Sharma who have become close friends!

Chapter 1, in part, is a reprint of the material as it appears in Optics Letters Vol 46 Issue 17 from 2021. Portions of the content in this chapter where originally in supplementary material of the original publication and have been edited into this format for clarity of the reader. The dissertation author was first author of this paper, with co-authors Hani Nejadriahi, Rajat Sharma, and Yeshaiahu Fainman.

Chapter 2, in part, is a reprint of the material as it appears in Optics Express. The dissertation author was the first author of this paper, with co-authors Dmitrii Belogolovskii, Andrew Grieco, and Yeshaiahu Fainman.

Chapter 3, in part is currently being prepared for submission for publication of the material with co-authors Dmitrii Belogolovskii, Andrew Grieco, and Yeshaiahu Fainman. The dissertation author was the first author of this material.

VITA

2016 Bachelor of Science in Electrical Engineering, San Diego State University

2022 Doctor of Philosophy in Electrical Engineering (Photonics), University of California San Diego

PUBLICATIONS

- **Alex Friedman**, Dmitrii Belogolovskii, Andrew Grieco, Yeshaiahu Fainman, "A systematic evaluation of Silicon-rich Nitride Electro-optic Modulator Design and Tradeoffs" Optics Express, *In Preparation*
- **Alex Friedman**, Dmitrii Belogolovskii, Andrew Grieco, Yeshaiahu Fainman, "Thermo-optic bistability in PECVD Silicon-Rich Nitride." Optics Express, *Accepted for Publication*
- **Alex Friedman**, Hani Nejadriahi, Rajat Sharma, and Yeshaiahu Fainman. "Demonstration of the DC-Kerr effect in silicon-rich nitride." Optics Letters 46, no. 17 (2021): 4236-4239.
- Hung-His Lin, Rajat Sharma, **Alex Friedman**, Benjamin M. Cromey, Felipe Vallini, Matthew W. Puckett, Khanh Kieu, and Yeshaiahu Fainman. "On the observation of dispersion in tunable second-order nonlinearities of silicon-rich nitride thin films." APL Photonics 4, no. 3 (2019): 036101.
- Hani Nejadriahi, **Alex Friedman**, Rajat Sharma, Steve Pappert, Yeshaiahu Fainman, and Paul Yu. "Thermo-optic properties of silicon-rich silicon nitride for on-chip applications." Optics Express 28, no. 17 (2020): 24951-24960.
- Naif Alshamrani, Andrew Grieco, **Alex Friedman**, Karl Johnson, Myun-Sik Kim, Francesco Floris, Peter O'brien, and Shaya Fainman. "A Non-Mechanical Multi-Wavelength Integrated Photonic Beam Steering System." Journal of Lightwave Technology (2020).

ABSTRACT OF THE DISSERTATION

Silicon-rich Nitride as a versatile and highly non-linear CMOS compatible material platform.

by

Alex Friedman

Doctor of Philosophy in Electrical Engineering (Photonics)

University of California San Diego, 2022

Professor Yeshaiahu Fainman, Chair

Silicon based photonic devices and systems are bringing a wealth of new capabilities and will continue towards large scale adaption in a variety of applications such as chip-chip communication. Such optical interconnects rely upon modulators as one of the key backbones in the interconnect link. Despite the growing importance of such interconnects however, CMOS compatible platforms still predominately utilize carrier dispersion-based modulators. Such

modulators rely upon the plasma dispersion effect in which changes in electron and hole concentrations drives a change in the refractive index of the junction region of typically a PN or PIN junction device. This approach while a clearly successful one, has a number of drawbacks such as its undesirable impact on not only the real but also imaginary part of the refractive index, but also typically results in high propagation losses, with higher modulation speeds requiring higher dopant concentrations and thus resulting in further loss increases. The optimal candidate for modulation then has is likely electro-optic modulators as utilizing the Pockels effect, based on the second order nonlinear susceptibility can enable pure real part changes in the refractive index. The most commercially successful electro-optic modulator being the commonly available, typically bulk, lithium niobate modulators. While materials such as lithium niobate, barium titanate, and others, can result in large changes in refractive index, and thus make efficient modulators, these materials are not compatible with the CMOS process flow. As such applications which strictly utilize CMOS process flows in tapeouts still mostly utilize carrier dispersion-based modulators.

In this thesis we will discuss Silicon rich nitride as a material platform. Why it is interesting, how it could bring new and powerful capabilities to a CMOS process flow, and why it deserves further exploration and adoption. We will discuss how Silicon-rich Nitride can be utilized in a variety of nonlinear applications, from modulation to optically bistable operation.

Our research has focused on exploring nonlinearities in a material platform readily compatible with CMOS process flows. Specifically, our research has centered around Plasma Enhanced Chemical Vapor Deposition (PECVD) based silicon rich nitride films. It has been shown in literature that such films can exhibit a wide range of refractive index values ranging from stochiometric films as low as approximately 1.87 up to as high as 3.1 and that such changes

in refractive index are reflective of its change in silicon concentration and nonlinear parameters. Such work in literature has shown that increases in silicon concentration result in increased second and third order nonlinear susceptibilities $\chi^{(2)}$ and $\chi^{(3)}$ respectively. In this thesis we have focused on exploring these nonlinearities in high refractive index CMOS compatible PECVD films. Our work has restricted itself to utilizing such fabrication flow, including low temperature deposition and annealing processes, in order to understand how such films, if adopted into CMOS process flows, could provide new and unique capabilities.

INTRODUCTION

The search to identify novel nonlinear optical materials compatible with CMOS manufacturing process to enable various on-chip Si-Photonic applications remains an area of active research. The second order ($\chi^{(2)}$) nonlinearity is not only the strongest among optical nonlinearities but also far more versatile and is used in electro-optic modulation and switching, frequency up/down conversion, and parametric processing. In the past years studies in literature have focused on exploiting materials which exhibit large second order nonlinear susceptibilities such as lithium niobate as well as high-k ferroelectric perovskites such as barium titanate. These approaches have resulted in efficient electro-optic devices driven by a need for solutions in particular applications, however, there remains a challenge in their integration into the CMOS process. The natural choice then would seem to be silicon; however, being a centro-symmetric material, it does not exhibit a second order nonlinear susceptibility and has limited power handling capabilities in non-linear optics applications in telecommunication spectral range due to its large two-photon absorption (TPA) coefficient. For modulation and switching then, many applications still rely upon carrier dispersion-based techniques where changes in electron and hole concentrations drive a change in refractive index; however, such techniques can only achieve limited speeds and typically produce large excess losses due to the increasing high dopant concentrations needed. An alternative approach is to exploit and engineer optical nonlinearities in an existing CMOS compatible Silicon Nitride (SiN) material platform. Specifically, Silicon-rich Nitride (SRN) films were demonstrated to have low loss, high refractive index with enhanced second ($\chi^{(2)}$) and third ($\chi^{(3)}$) order nonlinear susceptibilities and minimal TPA at telecommunication wavelengths. As such our approach has been to investigate the usage of such films, to find how effectively they can be utilized in a variety of nonlinear devices and systems,

with the goal in mind demonstrating that if adopted into the CMOS process flow, requiring minimal changes, that silicon-rich nitride films could be a valuable addition and bring pure real part modulation to the CMOS platform. What follows is a brief summary of the content of this work:

Chapter 1: We explore the deposition technique and resulting properties of PECVD based silicon-rich nitride films

- Demonstrate that low temperature PECVD techniques can result in low loss silicon-rich nitride films with refractive indices as high as 3.1
- Characterize the RF permittivity of such films
- Discuss the tensorial nature of $\chi^{(2)}$ and $\chi^{(3)}$ in Silicon-rich Nitride
- Characterize the $\chi^{(2)}$ and $\chi^{(3)}$ of Silicon-rich Nitride
- Characterize the maximum safe operating voltage (breakdown field) of these PECVD silicon-rich nitride films

Chapter 2: We demonstrate and explore optical bistable operation in PECVD Silicon-rich Nitride

- Demonstrate optical optically induced resonance shift with a linear dependance on on-chip optical power
- Demonstrate thermally induced resonance shift with a linear dependance on temperature
- Compare Optically and Thermally induced resonance shifts
- Measure the time response of the optically induced resonance shift to show that the effect is thermal in nature.
- Demonstrate optical bi-stability showing there is a region of input optical powers where two different output powers are possible.

- Demonstrate optically bi-stable operation and show the ability to switch between two stable optical states.

Chapter 3: We present a systematic evaluation of Silicon-rich Nitride Modulator design and tradeoffs

- Discuss the full expansion of the nonlinear polarizability in an arbitrary material
- Show how linear electro-optic modulation can be achieved with a heterodyne gain utilizing a combination of $\chi^{(2)}$ and $\chi^{(3)}$ in silicon-rich nitride and present the derived expression for the various contributions to the change in refractive index
- Present a proposed structure for the electro-optic modulator based on a set of GSG electrodes and shield layer
- Discuss the tradeoffs between TE and TM operation
- Present the analysis for the performance of a TM operated phase modulator based on the proposed structure
- Present the analysis for the operation of the proposed phase modulator for use as an intensity modulator in both a ring resonator (resonant) and Mach Zehnder (non-resonant) configurations
- Discuss the trade-offs inherent in ring resonator intensity modulator designs
- Discuss the trade-offs inherent in Mach Zehnder intensity modulator designs
- Discuss how such a PECVD Silicon-rich Nitride modulator compares to other material platform and modulation techniques as well as which of them are compatible with CMOS process flows

Background

The search for ever more efficient devices to power the next generation of optical interconnects has long been a driving force behind research in nonlinear optics. Recent studies have focused on exploiting the lithium niobate on insulator platform [1] as well as high-k ferroelectric perovskites such as barium titanate ($BaTiO_3$) [2] in order to realize more efficient electro-optic switches, however, the low refractive index, relative to silicon, and high RF permittivity remain a challenge for these platforms. Furthermore, the strong push towards CMOS compatible fabrication has continued to drive interest in CMOS compatible alternatives for realizing electro-optic switches. The natural choice would be to use a material (or its variant) and an effect that is already available as part of the current silicon photonics platform, such as the plasma dispersion or the DC-Kerr effect. Plasma dispersion-based switching is a commonly utilized technique in the Silicon-On-Insulator (SOI) platform; however, for many applications an ultra-low energy per bit metric is required making all-phase modulation desirable.

An alternative to directly utilizing silicon is to engineer optical nonlinearities in existing CMOS compatible materials. An attractive candidate for this is non-stoichiometric silicon nitride, and in particular Silicon-rich Nitride. A variety of deposition techniques, including but not limited to Inductively Coupled Plasma Chemical Vapor Deposition (ICP-CVD), Plasma Enhanced Chemical Vapor Deposition (PECVD), and Low-Pressure Chemical Vapor Deposition (LPCVD) have all been used to demonstrate low loss SRN film with enhanced second and third order nonlinear susceptibilities ($\chi^{(2)}$ and $\chi^{(3)}$) [3, 4, 5]. Using these deposition techniques, silicon-rich nitride (SRN) films have demonstrated efficient four-wave mixing where in the case of ultra-silicon-rich nitride $\chi^{(3)}$ coefficients as high as 1.02 x 10^{-18} m^2/V^2 have been demonstrated [4, 6].

By comparing this to recent work [7] in silicon where DC-Kerr based modulation was demonstrated using a $\chi^{(3)}$ of 2.45 x 10^{-19} m^2/V^2, the conclusion is that ultra-silicon rich nitride has a variety of highly desirable characteristics for electro-optic switching and the exploration of the DC-Kerr effect in this platform deserves consideration.

In this manuscript we will discuss how SRN possess several advantages which make it a strong candidate for practical switching applications. Specifically, we report a PECVD grown SRN film with a refractive index of 3.02 at 1500nm and experimentally demonstrate a $\chi^{(3)}$ as high as (6 ± 0.58) x 10^{-19} m^2/V^2. Additionally, we make the argument in favor of PECVD based deposition of SRN over other deposition methods as a technique readily available in CMOS process flows for realizing highly nonlinear SRN films for electro-optic switching applications.

Theory

As introduced in the previous section, plasma-dispersion is commonly utilized for modulation and switching applications in silicon; however, this technique produces, an often un-desirable, change in the imaginary part of the refractive index as well as the real part [8]. An alternative to plasma dispersion is to utilize the Pockels effect [9], such as is exploited by Lithium Niobate modulators [1]. However, due to central crystal symmetry silicon does not possess a $\chi^{(2)}$. As an alternative to this, the DC-Kerr effect has recently been demonstrated in Silicon utilizing a p-i-n junction configuration [7]. This has been demonstrated to be an effective method for realizing electro-optic modulation in silicon. However, its realization has currently been limited to p-i-n junction configurations as a means of overcoming the challenges of engineering efficient overlap of the electric field with the optical mode within a semiconductor. The i-th component of the refractive index modulation, Δn_i due to DC induced Kerr effect is given by,

$$\Delta n_i = \frac{3\,\Gamma_{SRN}}{2}\sum_{j,k,l}\frac{\chi^{(3)}_{ijkl}}{n_{l,eq}}E^{dc}_j E^{dc}_k \quad ,(1.1)$$

where $\Gamma_{SRN}, n_{l,eq}$, $\chi^{(3)}_{ijkl}$, E^{dc}_j, and E^{dc}_k represent the overlap factor, the unperturbed material index of the "lth" polarization, "ijkl" tensor component of the $\chi^{(3)}$, the jth and kth component of the applied electric field, respectively. The utilization of electrodes in a top-down configuration, with a grounded substrate, results in an applied electric field (E^{dc}_j) which is predominately aligned normal to the thin SRN film which along with isotropic material symmetry allows equation 1.1 to be reduced to equation 1.2.

$$\Delta n_i = \frac{3\,\Gamma_{\mathrm{SRN}}}{2}\sum_{i,j}\frac{\chi^{(3)}_{ijji}}{n_{i,eq}}E^{dc^2}_j \qquad (1.2)$$

It should further be noted that for SRN's material class only certain tensor components will be non-zero, additionally due to our choice to utilize a TM- polarized optical mode the only participating non-zero tensor component is the $\chi^{(3)}_{3333}$. It is evident that with this approach we can achieve electro-optic switching in any material platform regardless of its crystal symmetry, as long as the given material has a large enough combination of $\chi^{(3)}$ and high electric breakdown field strength. However, in SRN the overall change in the material index is often a combination of both second and third order contributions, due to the Pockels and DC-Kerr effects respectively, even if the second order contributions are often small [5]. As such an accurate estimate of the $\chi^{(3)}$ requires consideration for the contributions of both these terms due to the presence of a non-zero $\chi^{(2)}$. For these reasons, SRN becomes a very attractive candidate. Specifically, it has been shown in literature that SRN thin films can exhibit very high third order nonlinear susceptibilities, even larger than that of silicon itself [5], have a higher breakdown field [10], while remaining a low loss dielectric waveguiding material [11,12]. It is for this reason that SRN deserves strong

consideration as a candidate platform for electro-optic switching. In the following, we carry out electro-optic measurements of the nonlinear optical response of these films used as a wave guiding material.

Design and Fabrication

In this work we choose to utilize a bus-coupled racetrack ring resonator and a TM-polarized optical mode to carry out electro-optic characterization of the all-normal components of the SRN film's susceptibility tensors (see Fig 1(a)). Details of the PECVD SRN film deposition are outlined in our previous work [13]. In parallel we also prepared samples of Au-SRN-Au capacitors in order to confirm the safe operating range of electric fields for these films. From these measurements we confirm our films to be safe for application of fields up to 1.2×10^8 V/m, which is in line with electric field breakdown strength measurements that have been carried out on SRN films with similar silicon compositions [14] and approximate our films RF permittivity to be 9.0578. Ellipsometric measurements performed at a wavelength of 800 nm confirm our films to increase in refractive index when they undergo rapid thermal annealing (RTA) at 300°C [15]. Furthermore, ellipsometry results confirm the refractive index to be 3.01896 at 1500nm, the methods of which are the same as in [13]. Our device architecture uses a 320 nm thick PECVD SRN device layer on top of a 3 μm wet thermal oxide on a silicon handling wafer. The device consists of a point-coupled racetrack ring resonator with a bend radius of 45 μm and straight arm sections of 250 μm. All such resonators have a waveguide width of 450 nm and coupling gaps ranging from 100 nm to 400 nm. The device geometry is written by electron beam lithography in a 400 nm thick fox-16 soft mask followed by dry etching using reactive ion etching in an Oxford P100 etcher. After etching, the remaining fox-16 is removed using 1:10 Buffered Oxide Etchant

diluted in D.I. water. The devices are then cladded with a 1 μm thick layer of PECVD SiO_2. Electrode traces 30 μm wide with a 10 μm separation are then patterned on top of the top clad using an AZ1512/SF9 bi-layer soft mask and DC sputtering of gold in a Denton 635 sputtering system. These samples then undergo RTA at 300°C in a forming gas ambient for 15 mins. The devices are then diced to expose the edge facets of the waveguides.

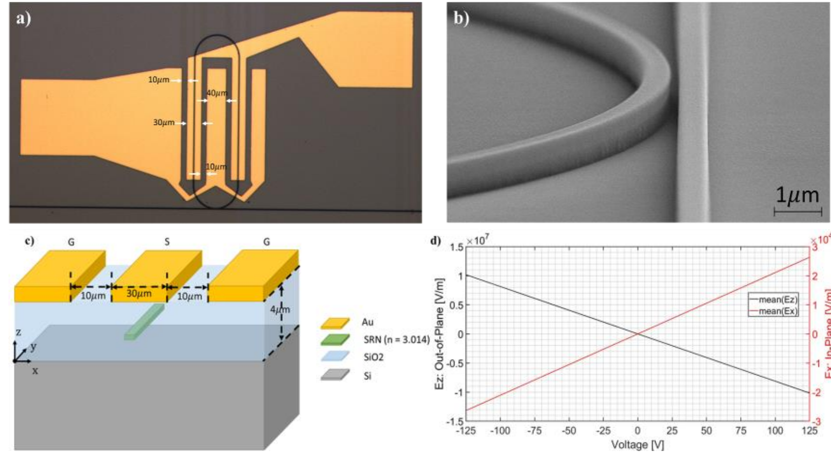

Figure 1: (a) Optical microscope image of our point coupled ring resonator with electrode width and spacing marked with white arrows and text overlay. (b) Scanning Electron Microscope image of the point coupler region of a racetrack ring resonator with the FOX-16 on top of the post etched waveguides. (c) Schematic breakdown of the phase shifter design shown as a cutout. Note that the substrate of the sample is also grounded. (d) Simulation Results for the mean value of the Applied Field Ex and Ez components versus voltage inside the waveguide core.

The electrode design plays an important role in our study, as we wish to be able to attribute our measurements to specific tensor components, in order to do this, we need to ensure a uniform and directional distribution of the applied DC electric field. Figure 1(c) shows the electrode design while figure 1(d) shows simulation results demonstrating that by using a wide central trace along with grounding the sample substrate the applied field distribution can be made to have as much as a 3 order of magnitude difference between the in-plane and out-of-plane applied fields. This allows us to uniquely attribute our electro-optic measurements of the TM-like polarized optical mode to the $\chi^{(3)}_{3333}$ tensor component.

Characterization Technique and Experimental Results

For characterization we use a fiber coupled input, free-space output setup with a tunable Agilent 8164B CW source which has a wavelength span of 1465 nm to 1575 nm [5]. Electrical probes are used to contact the electrical pads (see figure 1.1(a)) applying voltage from a Keithly Source Meter 2400 with a maximum voltage range of $\pm$210 V.

To characterize the DC-Kerr effect, transmission spectra measurements are taken as a function of applied voltage. Using these spectral measurements, the shift in resonant wavelength versus voltage can be extracted. This measurement of resonant wavelength shift ($\Delta\lambda_{res}$) versus voltage can then be related to the change in effective index (Δn_{eff}) on a first order approximation using equation 1.3 below as a ratio of the group index (n_g) and the resonant wavelength (λ_{res}) scaled by the modulated length of the ring (L_{mod}) as a fraction of total length of the ring (L_{total}), 440 μm and 782.74 μm respectively [16,17]. An important note is that as was discussed previously, our choice to use electrodes in a top-down configuration ensures we have an all-vertical applied field. Thus, when these measurements are carried out for a TM-like optical mode this allows us to attribute our measurements entirely to the all-normal type $\chi^{(2)}_{333}$ and $\chi^{(3)}_{3333}$.

$$\frac{\Delta n_{eff}}{n_g}\frac{L_{mod}}{L_{total}} = \frac{\Delta\lambda_{res}}{\lambda_{res}} \qquad (1.3)$$

The results of these measurements are shown in figure 2 (a) - (c). These measurements are used to determine $\chi^{(2)}_{333}$ and $\chi^{(3)}_{3333}$ by fitting for the change in effective refractive index as a function of applied field using Lumerical mode simulations to solve for the effective refractive index of the guided mode as function of change in spatial dependent material index for the waveguide core. This spatial dependent material index is derived from modeling of the applied field within the waveguide core as a function of applied field using Lumerical Device. In this way

a best fit optimization is done to determine $\chi^{(2)}_{333}$ and $\chi^{(3)}_{3333}$ from the measurements, the results of which can be seen in figure 2(c).

The propagation loss of the circulating mode can be seen extracted from figure 2(a) by fitting the measured response to the Lorentzian equation as in [13,17] and results in an in-waveguide propagation loss of 3.41 dB/cm for the TM-like polarization. This is done by performing a best fit optimization in order to fit the experimental results to the analytical formula for an all-pass ring resonator shown in [16]. Additionally, the free-spectral range of the racetrack resonator is found to be 0.756 nm which corresponds to a group index of 3.803 [13]. The results of the TM-like active optical measurements of resonant wavelength shift versus voltage can be seen in figure 2(b) with figure 2(c) showing the resulting change in effective index versus voltage using equation 3. Figure 2(c) shows the fit for $\chi^{(2)}_{333}$ and $\chi^{(3)}_{3333}$ resulting in values of (14.5 $\pm$ 1.4) pm/v and (6 $\pm$ 0.58) x 10^{-19} m^2/V^2 respectively. In figures 2(b) and (c) we observe a clear quadratic dependence of the change in resonance wavelength, and change in effective index, on the applied voltage with the minima point displaced from the origin due to the presence of a non-zero $\chi^{(2)}_{333}$ in as grown SRN films. The uncertainty in the $\chi^{(2)}$ and $\chi^{(3)}$ is primarily due the relative wavelength accuracy of the tunable Agilent 8164B CW source used in our measurements. The relative wavelength accuracy of our Agilent 8164B CW source is $\pm$ 3 pm, resulting in an uncertainty in Δn_{eff} of $\pm$ 1.35 x 10^{-5}.

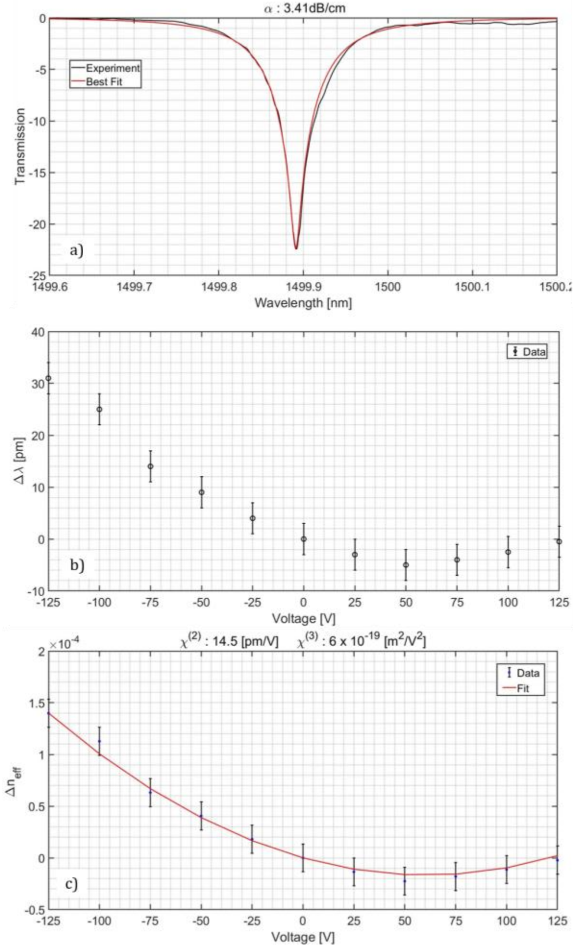

Figure 2: Above the top cladding there are electrodes 220 μm in length on each of the two straight arm sections. All measured data is operated in the TM polarization for a 320 nm thick 450 nm wide SRN waveguide. (a) Measurement of the transmission versus wavelength along with the best fit for a single resonance showing the propagation loss of the circulating mode. (b) Shift in resonance wavelength in pico-meters versus applied voltage. (c) Change in effective index versus applied voltage along with the best fit results resulting in a $\chi^{(2)}_{333}$ of (14.5 $\pm$ 1.4) pm/v and a $\chi^{(3)}_{3333}$ of (6 $\pm$ 0.58) x 10^{-19} m^2/V^2.

Comparing these results to other works in literature [12,18-22] we find our SRN film to be in line with predictions made in the literature based on the relationship between a SRN film and the $\chi^{(3)}$ it will exhibit [4]. Additionally, we find the $\chi^{(3)}$ of our films to exceed that of Silicon. Furthermore, the clear shift in the minimum point in change in refractive index versus voltage confirms the presence of a combination of second and third order nonlinearities as shown in the fitting results.

Conclusion

In this work we have presented a PECVD based SRN film with a refractive index of 3.02 at 1500 nm, achieved an in-waveguide propagation loss of 3.41 dB/cm for the TM-like polarized optical mode. We have also shown that SRN films, in contrast to highly nonlinear materials such as $BaTiO_3$ [23], can retain a low RF permittivity of 9.0578 when deposited using PECVD. Additionally, in this work we have maintained all processing steps at a temperature of 350°C or below. While it is true that lower-loss highly nonlinear SRN films have been demonstrated in literature, existing work has primarily focused on LPCVD and ICP-CVD [12,24,25]. In comparison to these techniques PECVD has a major advantage, readily available compatibility with CMOS process flows and maintains a low thermal budget compared to LPCVD, which are typically deposited at temperatures as high as 800°C and undergo long annealing processes at temperatures as high as 1200°C.

Using the DC-Kerr effect we have experimentally measured the $\chi^{(3)}_{3333}$ of our SRN film to be (6 $\pm$ 0.58) x 10^{-19} m^2/V^2 for the TM-like polarized optical mode in the presence of a vertical applied field. The DC-Kerr effect in SRN is used as an optical phase shifter for tuning of a ring-resonator device. This technique can offer an alternative mechanism for employing optical phase shifters in SRN films. Furthermore, PECVD SRN is a highly tunable material which allows a designer to control its refractive index [4], thermo-optic coefficient [13], as well as second and third order nonlinear susceptibilities [3-5] while maintaining low loss and two photon absorption with breakdown field strengths superior to that of silicon [4]. Additionally, when processed using PECVD, a low thermal budget can be maintained using a deposition technique readily available in CMOS process flows. As such, SRN is a very promising material platform which deservers further

exploration for on chip applications towards highspeed electro-optic switches, analog transmitters and microwave photonics.

Supplementary topic: Tensor Analysis of the Quadratic Electro-optic Effect.

Below a more complete expansion showing the terms omitted from the expansion of the nonlinear polarizability can be seen below. Note that here subscripts denoting the tensorial nature of $\chi^{(2)}$ and $\chi^{(3)}$ have been suppressed.

$$\text{(a)} \qquad \bar{P} = \epsilon_0\{\chi^{(1)} + \chi^{(2)}\bar{E} + \chi^{(3)}\bar{E}^2\}\bar{E}$$

$$\text{(b)} \qquad \bar{E} = \bar{E}_{dc} + \bar{E}_{\omega} = \bar{E}_{dc} + Ee^{-j\omega t} + E^*e^{j\omega t}$$

Thus

$$\text{(c)} \qquad \bar{P}_{Electrostatic2} = \epsilon_0\chi^{(2)}[2EE^* + E_{dc}^2]$$

$$\bar{P}_{Pockels} = \epsilon_0\chi^{(2)}[2E_{dc}Ee^{-j\omega t} + 2E_{dc}E^*e^{j\omega t}]$$

$$\bar{P}_{SHG} = \epsilon_0\chi^{(2)}[E^2e^{-j2\omega t} + E^*e^{j2\omega t}]$$

$$\bar{P}_{Electrostatic3} = \epsilon_0\chi^{(3)}[E_{dc}^3 + 6EE^*E_{dc}]$$

$$\bar{P}_{Kerr} = \epsilon_0\chi^{(3)}[3E^2E^*e^{-j\omega t} + 3EE^{*^2}e^{j\omega t}]$$

$$\bar{P}_{DC-Kerr} = \epsilon_0\chi^{(3)}[3E_{dc}^2Ee^{-j\omega t} + 3E_{dc}^2E^*e^{j\omega t}]$$

$$\bar{P}_{EFISHG} = \epsilon_0\chi^{(3)}[3E_{dc}E^2e^{-j2\omega t} + 3E_{dc}E^{*^2}e^{j2\omega t}]$$

$$\bar{P}_{THG} = \epsilon_0\chi^{(3)}[E^3e^{-j3\omega t} + E^{*^3}e^{j3\omega t}]$$

(a) Expansion of the Polarizability up to third order contributions. (b) Assumed Electric field distribution as a summation of a low frequency (relative to the optical mode) contribution and the optical mode written as a Bloch wave. (c) Resulting expansion of the nonlinear terms of the polarizability organized and labeled to show what effect each set of terms results in. Pay special attention to the similarity between the quadratic electro-optic effect and the Pockels effect terms.

In the above expansion the overall electric field has been modeled as a summation of the optical wave and an electro-static field. The Optical Mode has then been expressed as a Bloch wave along with its complex conjugate. Relevant terms in this expansion, such as the $\bar{P}_{DC-Kerr}$ term can then be related to an index change in material index by refactoring that individual term to appear as an effective first order change in linear susceptibility, which is the related to a change in refractive index by $n^2 = \epsilon_r = \chi^{(1)} + 1$. Doing so and re-introducing the subscripts for the tensorial nature of this phenomena, we can arrive at the following.

$$\text{(d)} \qquad \Delta n_i = \frac{3\Gamma_{SRN}}{2} \sum_{i,j,k,l} \frac{\chi^{(3)}_{ijkl}}{n_{l,eq}} E^{dc}_j E^{dc}_k$$

Due to symmetry and imposed field conditions:

$$\text{(e)} \qquad \Delta n_i = \frac{3\,\Gamma_{\mathrm{SRN}}}{2} \sum_{i,j} \frac{\chi^{(3)}_{ijji}}{n_{i,eq}} E^{dc^2}_j$$

(d) The change in linear refractive index due to the DC-Kerr term in the general case. Note the subscripts (i,j,k,l) can be 1,2 , or 3 and are used to refer to one of the three coordinate axis (x,y, or z). The term Γ_{SRN} is the model overlap factor with the Silicon-Rich Nitride material. (e) Given the restrictions on the applied field distribution imposed by our choice of electrodes the applied electro-static field contains a single vector component, and this allows us to simply the expression as shown.

(d) shows the resulting expression for the change in refractive index due to the DC-Kerr effect in the general case of a material with a $\chi^{(3)}_{ijkl}$ under an arbitrarily oriented electro-static field for an optical mode of a given polarization. Part (e), shows a simplified form of the equation for the geometry explored in this manuscript in the Silicon-Rich Silicon Nitride material platform.

Supplementary Topic: Extraction of RF Permittivity and Breakdown Field

In order to properly characterize the Silicon-Rich Nitride thin films it is important to determine the RF permittivity and carry out some preliminary measurements of the breakdown field of the SRN thin films. First, it would be an advantage to have the Silicon-rich Nitride thin films exhibit as low of an RF permittivity as possible allowing for efficient application of the applied electric field. Second, the higher the breakdown field the higher the potential change in linear refractive index achieved. In order to determine both parameters we fabricate parallel plate capacitors of two different areas using a 150nm thick layer of our Silicon-rich Nitride thin film.

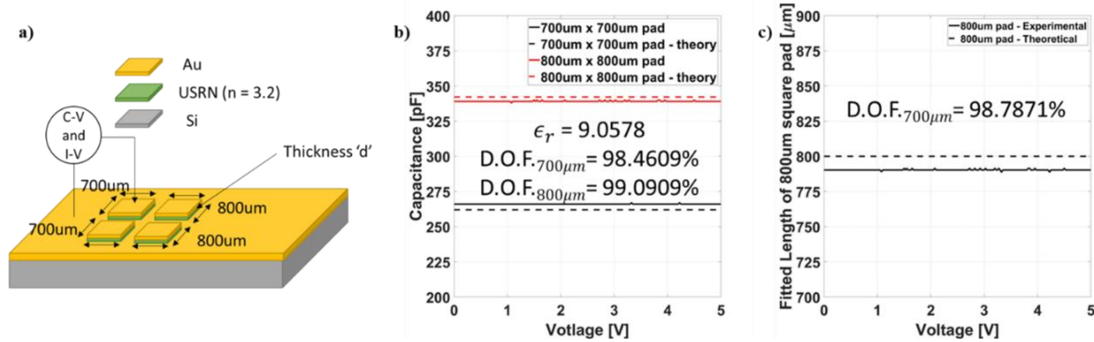

Figure 3: (a) Schematic breakdown of the test structure used to extract the RF permittivity. Capacitance vs voltage measurements are performed using an Agilent B1500A semiconductor device analyzer. Thickness 'd' = 150nm. (b) Capacitance [pF] vs Voltage [V] at 100 kHz along with a fitting for the relative permittivity showing a value of 9.0578. (c) Confirmation of the fitting where the effective length [μm] of one pad is extracted based on fitting the other pad for its relative permittivity. As can be seen the fitting is good using either method and show similar results.

Here, one can see the extraction of the RF permittivity of the film, done by performing a capacitance vs voltage measurement using an Agilent B1500A semiconductor device analyzer. The results for 700μm x 700μm and 800μm x 800μm square pads simultaneously fit to extract the RF permittivity. The relative length of one pad is fit based on the results extracted from a single pad, which serves to confirm our measurement. From this fitting we find the RF permittivity to be 9.0578, which is a little less than the linear refractive index squared. This is an important result as

it confirms that despite have a high linear refractive index and third order nonlinear susceptibility, these films still exhibit a relatively low RF permittivity.

We utilize a current (I) vs voltage (V) measurement to determine the point of maximum safe electrical field strength for our Silicon-rich Nitride thin films. I-V measurements were used both pre- and post-anneal (at 300°C) by increasing the voltage until the current spikes to the pre-set compliance. From these preliminary measurements we concluded that annealing these films does improve the maximum safe field point, with post anneal being 1.2 x 10^8 [V/m] as opposed to 8.3 x 10^7 [V/m] pre-anneal.

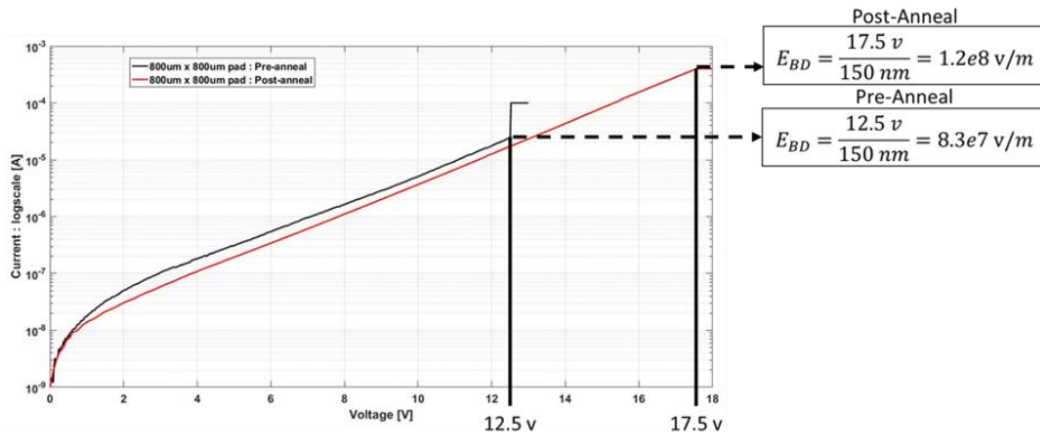

Figure 4: Current [A] vs voltage [V] up to the point of breakage plotted on a semilog scale both pre- and post- anneal at 300°C. As can be seen, annealing of these films does improve the maximum safe electric field strength with post annealing is 1.2 x 10^8 [V/m] as opposed to 8.3 x 10^7 [V/m] pre-annealing.

Supplementary Topic: The effects of annealing on Silicon-rich Nitride

Building upon the demonstration of electric field induced second harmonic generation in Silicon-rich Nitride thin films from [5] we set out to further increase the silicon content of these films. As before we deposit these films using plasma enhanced chemical vapor deposition (PECVD), making sure to remove the ammonia flow from the process we settle on a recipe with a silane to N2 gas flow ratio of 2.25. With this we deposit 320nm thick films of Silicon-rich Nitride onto a 3μm wet thermal on silicon substrate. Due to the fact that these devices will eventually be

clad with a PECVD SiO_2 layer it is important to understand the effects that annealing in forming gas will have on our thin films, furthermore annealing any PECVD deposited dielectric is an important step in achieving true high quality thin films. Therefore, the effects of annealing in a forming gas ambient are quantified as a function of annealing temperature.

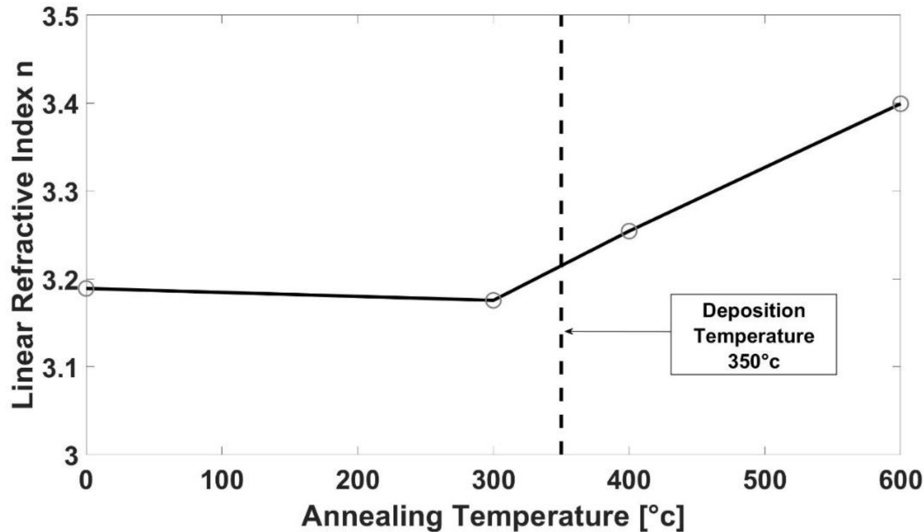

Figure 5: A plot of Linear refractive index at a wavelength of 800nm using ellipsometry as a function of annealing temperature. All films where deposited at the same time at 350°C. These films were then individually annealed for 15 mins in a forming gas ambient at the listed temperature. As expected, increasing the annealing temperature beyond the deposition temperature results in an increase in the linear refractive index [11].

In all of the above cases the annealing is done for 15 mins in a forming gas ambient at the given temperature. As expected, annealing of Silicon-rich Nitride above its deposition temperature for PECVD films results in an increase in the linear index of the film. From this data we can conclude that we can anneal these films at 300°C for 15mins in forming gas in order improve the general quality of our eventual SiO_2 top cladding as well as our Silicon-rich Nitride thin film, without significantly effecting the linear refractive index of the films. With this confirmation we will then follow the same process flow as shown previously in [1], finishing by annealing our 1μm SiO2 top cladding layer for 15mins at 300°C in a forming gas ambient.

Supplementary Topic: Electrode Design

The design of the electrodes is chosen to ensure a uniform and highly directional field distribution. This is important because it will allow us to conclusively relate our measurements to a specific combination of tensor components in Silicon-Rich Nitride.

As can be seen in figure 6(a), we choose to electrode traces 30μm wide separated by 10μm along with a grounded substrate. By maximizing the width of the electrode traces as well as choosing a thickness for the SiO2 top clad we can ensure a highly uniform and predominately vertical applied field distribution within the waveguide. Here we chose to utilize a 1μm SiO2 top cladding balancing the need for low loss waveguiding with applied field strength within the waveguide core. The electrode width and spacing was chosen to be 30μm and 10μm respectively, for a waveguide width of 400nm. The applied field distribution is determined by modeling in Lumerical Device.

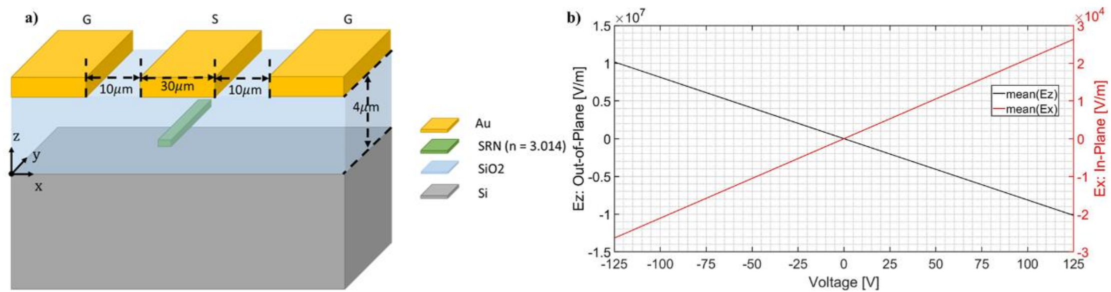

Figure 6: (a) A schematic breakdown of the phase shifter design shown as a cut out. The goal of this design is to have the applied field distribution to be as uniform and directional as possible. The electrode traces are 30μm wide electrode and separated by 10 μm. These electrodes are patterned using liftoff from an AZ1512/SF9 soft mask and dc sputtering in a Denton 635. (b) Plot of the mean value of the Applied Field Ex and Ez components versus voltage inside the waveguide core.

In figure 6(b), you can see the magnitude of the applied field distribution as a function of in-plane position vertically centered in the waveguide. From this plot we see that the in-plane component is more than three orders of magnitude smaller than the out of plane component. Due to this large difference between the in-plane and out-of-plane applied field components, second

order processes dependent on the in-plane applied field component can't contribute. Additionally, the squared dependence on applied field allows third order contributions to be safely ignored as there is a six-order difference in magnitude of its contribution as compared to that of the out-of-plane applied field.

The fact that we can safely ignore the in-plane applied field, and its effect on the refractive index, allows for us to conclude that the only two non-zero and participating tensor components of the third order nonlinear susceptibility are $\chi^{(3)}_{1331}$ and $\chi^{(3)}_{3333}$, see figure 7.

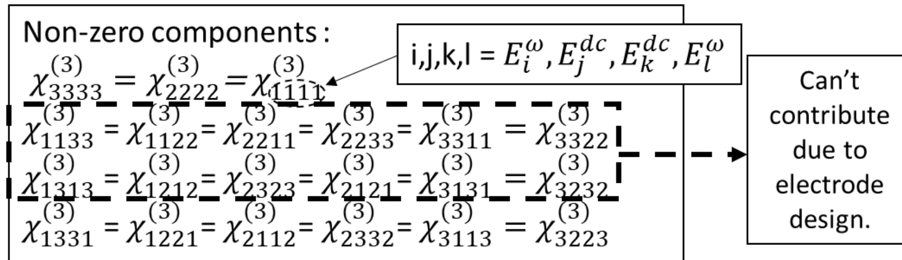

Figure 7: In isotropic media the above tensor components are the 21 non-zero elements. The subscripts 1, 2, and 3 represent the three-principle axis 'i', 'j', and 'k'. From our design of the electrodes we can conclude that any terms with mixed contributions from the applied field, labeled as 'Edc' along multiple axis can be neglected in our measurements. Furthermore, it is important to understand that the largest tensor component is expected to be the $\chi^{(3)}_{3333}$ component as it should be a summation of the three other non-zero, unique tensor components. More details on this can be found in [1].

Supplementary Topic: The interplay between $\chi^{(2)}$ and $\chi^{(3)}$ and its effect on Δn

The other sections here have focused primarily on the third order contributions; however, in general materials can exhibit both second and third order susceptibilities, depending on a materials crystal symmetry. For example, as-grown silicon-rich nitride has been shown to exhibit a second order nonlinear susceptibility which increases with increasing silicon content. As a result of this, the resulting Δn in such a material must be modeled as equation S3 below rather than as a purely quadratic change as is the case in centro-symmetric materials such as silicon.

$$\Delta n_i = \Gamma_{SRN} \sum_{j,k} \frac{\chi^{(2)}_{ijk}}{n_{k,eq}} E^{dc}_j + \frac{3\,\Gamma_{\mathrm{SRN}}}{2} \sum_{i,j} \frac{\chi^{(3)}_{ijji}}{n_{i,eq}} E^{dc^2}_j$$

In general, the change in refractive index of a material is the summation of all contributions from all higher order susceptibility terms across all tensor components. Depending on the material in question some of the tensor components may be zero and furthermore, depending on the orientation of the applied electric field others may not contribute.

As a result of the linear dependence of Δn on applied electric field due to the second order nonlinear susceptibility and quadratic dependance on applied electric field due to the third order nonlinear susceptibility, the minima of the Δn curve is shifted from 0v. In other words, materials which have a $\chi^{(2)}$ will exhibit asymmetry in their measured Δn(V) response unlike centro-symmetric materials such as silicon which will exhibit a purely quadratic (and thus symmetric) Δn(V) response. This is because for one polarity of applied electric field the contributions from $\chi^{(2)}$ is of the opposite polarity to that of the contributions from $\chi^{(3)}$ until they eventually cancel each other out after which contribution from $\chi^{(3)}$ overcomes $\chi^{(2)}$. On the other hand, for the opposite polarity these two contributions add up as they have the same sign in their contribution to Δn.

Acknowledgements

Chapter 1, in part, is a reprint of the material as it appears in Optics Letters Vol 46 Issue 17 from 2021. Portions of the content in this chapter where originally in supplementary material of the original publication and have been edited into this format for clarity of the reader. The dissertation author was first author of this paper, with co-authors Hani Nejadriahi, Rajat Sharma, and Yeshaiahu Fainman.

CHAPTER 2 – OPTICAL BISTABILITY IN PECVD SILICON-RICH NITRIDE

Background

Research towards optical logic components is an ongoing area of interest and optically bi-stable devices have been of keen interest in such research as they can provide a fundamental building block for optical logic gates [1-3]. In the past, optical bistability has been shown in silicon devices [4-9]; however, silicon nitride has become an attractive candidate for nonlinear optical processes due to its low-loss nature, low two-photon absorption, and as has more recently been shown, the capability to exhibit an enhanced third order nonlinear susceptibility. Existing work in literature exploring optical bistability in silicon nitride ring resonator devices has primarily focused on stoichiometric to low refractive index silicon nitride [10], both exploring the possibility of a Kerr based ultra-fast optically bistable ring resonator for use as a memory element [11] as well as in a variety of other novel applications such as for a photonic thermometer where thermo-optic bistability is exploited for temperature sensing [12]. In past work by the author's [13], as well as others in the literature [14-18], we have shown how by controlling the conditions during deposition, high silicon content silicon-rich nitride films can be deposited by PECVD and shown that these films exhibit enhanced second and third order nonlinear susceptibilities, thermo-optic coefficient, and refractive index while maintaining many of the benefits of silicon nitride films. Such films have been used in a variety of manners in literature such as for optical parametric amplifiers [19], for soliton-effect optical pulse compression [20], as well as pushes towards the fabrication of even higher composition films such as low temperature plasma-deposited dichlorosilane-based ultra-silicon-rich nitride films [21]. A useful overview of the various forms of silicon-rich nitride as a highly nonlinear CMOS platform can be found in [17].

In this manuscript we demonstrate and characterize thermo-optic bistability in a PECVD SRN with a refractive index of 3.02 at 1500nm for use as an optically bi-stable element. We compare optically induced resonance shifts to thermal heating induced shifts, as well as characterize its time response. Specifically, we determine the thermo-optic coefficient of our PECVD SRN film to be $(2.12 \pm 0.125)\times10^{-4}/{\circ}C$ by examining the optically induced resonance shift. We experimentally demonstrate bi-stable optical switching and measure the time response of the device showing the relaxation time to be approximately 18.7us. Finally, we make an argument for high refractive index PECVD SRN for use as optically bistable material in computing and sensing applications such as thermal sensing. Utilizing high refractive index PECVD SRN films for a variety of applications provides significant benefits over traditional utilization of low index or stoichometric nitride films [12] due to the much larger thermo-optic coefficient and higher confinement waveguide while maintaining a low loss guiding layer and negligible TPA [22].

Design and Fabrication

In this manuscript we characterize the thermo-optic properties of high refractive index PECVD SRN, demonstrating thermo-optic bistability in an all-pass ring resonator device operating in a TM- mode. It has been shown in the literature [10, 23] that when a laser of sufficient optical intensity is coupled on resonance into the cavity of a ring resonator, the absorbed portion of that optical intensity results in a change in temperature of the cavity which via the thermo-optic effect results in a shift of the resonant wavelength of the cavity. Modeling the change in refractive index resulting from a given optical power has been shown in [10-12, 23]. The relation between the intensity of the optical wave in the cavity and the self-induced change in refractive index, Δn in

time, *t* through induced temperature change and the film's thermo-optic coefficient is reproduced from Ref. 10 below:

$$\frac{d\Delta n}{dt} = \Delta n_a - \frac{\Delta n}{t_c} \qquad (2.1)$$

Here Δn_a and $\mathrm{t_c}$ are defined as, the linear accumulation term and the characteristic time constant respectively.

$$\Delta n_a = \frac{dndT\ I\ \alpha}{2\rho C_p} \qquad (2.2)$$

where $\frac{dn}{dT}$, I, α, ρ, and C_p are the thermo-optic coefficient, Intensity, absorption coefficient, density, and specific heat respectively,

$$\mathrm{t_c} = \frac{R^2 \rho C_p}{4k} \qquad (2.3)$$

where R and k are defined as the mode radius and thermal conductivity respectively. In the above $\rho \cong 2.2$g/cm^3, $C_p \cong 0.76\, J/gK$, k ≅ 0.0014 W/cmK are taken from literature references [10,12], while the mode radius R is taken to be the bend radius of the ring resonator cavity, $45\mu m$. The characteristic time constant $\mathrm{t_c}$ is both taken from measurements performed in section 5 and fit along with the unknowns $\frac{dn}{dT}$ and α, which is constrained by the overall propagation loss measured in section 3.

In this work we will explore this effect in high refractive index PECVD SRN, characterizing the thermo-optic coefficient by optical shift measurements as well as comparing it to a measurement of chip temperature. We will then perform time response measurements, estimate the relaxation time and deduce that it is indeed a thermal effect, as well as use this effect to demonstrate bi-stable optical switching.

Details of the PECVD SRN films deposition are described in our previous work [13]. Our device consists of a 311nm thick PECVD SRN device layer deposited onto 3um of wet thermal

oxide on a silicon handling wafer. Our device design consisting of an input and output grating couplers along with a 45um bend radius all-pass ring resonator is patterned into the SRN device layer using electron-beam lithography of a 150nm thick HSQ soft mask. The developed HSQ mask is then used to transfer the device structure into the SRN device layer using reactive ion etching in an Oxford P100 etcher. After etching any remaining HSQ is removed using 1:10 buffered oxide etchant diluted in DI water. The devices are then clad with 1.5um of PECVD SiO_2. Figure 8 below shows an optical microscope image of our SRN all-pass ring resonator device consisting of a 45um bend radius ring with a width of 385nm coupled to a bus waveguide of width 385nm separated by a gap of 100nm.

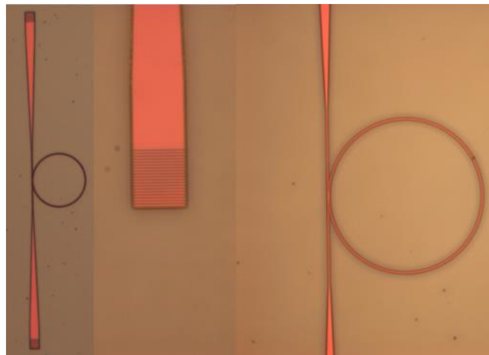

Figure 8: Optical microscope image of the PECVD SRN 45um bend radius all-pass ring resonator device.

Low-power Characterization

The transmission spectra from our SRN ring resonator device is first measured at low input optical powers in order to demonstrate that the spectra is symmetric at low input powers as well as determine the propagation loss and group index of our ring resonator device. To do so we couple an Agilent 81980B tunable laser to the input grating coupler and measure the output power using a Newport 918D-IG-OD3 detector connected to digital to analog converter and storage in the

computer. We can then determine the transmission spectra by sweeping the wavelength of the Agilent tunable laser source and measuring the output power over time using the laser's output trigger to calibrate the wavelength at each moment along the measurement (more details on the measurement method can be found in our past work [13]).

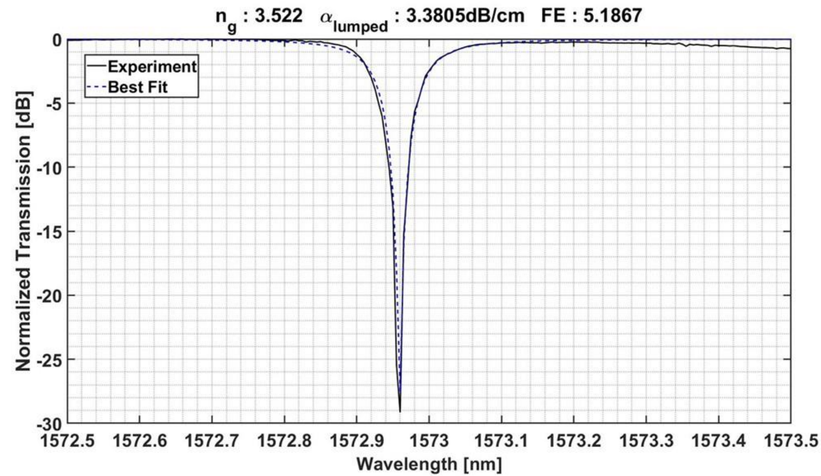

Figure 9: Normalized transmission spectra at low input power for the SRN ring device operating in the TM-like mode. Shown is a fitting for the transmission spectra's line shape we determine the propagation loss to be 3.38dB/cm for a group index of 3.522 ± 0.156.

Figure 9 shows the resulting normalized transmission spectra for the SRN ring resonator device operating in the TM-like mode. By fitting the transmitted optical spectra to a well-known line shape function, as in [24-25], using a root mean square fitting we can determine the propagation loss of the circulating mode, the group index, and the self-coupling coefficient of the bus waveguide. The results of the root mean square fitting of a single resonance can be seen as the blue dashed line in Figure 2 corresponding to a group index of 3.522 ± 0.156, note that the FSR which is measured to be 2.38nm corresponds to a group index of 3.677 while a fitting of the single resonance on indicates as low as 3.3657, such uncertainty is considered in the margins of error presented on the fitted parameters as proper analysis of the resonances is harder in the nonlinear regime. A propagation loss of 3.38 dB/cm is found, with a self-coupling coefficient of 0.957 and

a cross-coupling coefficient of 0.291. From this we estimate the field enhancement factor (FE) to be 5.1867 [10-12]. Additionally, it is important, to note that this loss value is the propagation loss of the mode circulating in the ring and thus includes all forms of loss such as bending, scattering, and absorption losses. Additional information on typical loss values in silicon-rich nitride films by the authors past works can be found in [13,14] with a more comprehensive view [17] as well as discussion on the usage of post-process annealing in LPCVD silicon-rich nitride films in [22]. As can be seen from these results under low input powers the line shape is symmetric indicating negligible contribution from self-induced thermo-optical bistability. Additionally, comparing these results to that of straight waveguides connected by grating couplers of the same design we estimate the insertion loss per grating coupler to be ~9.5dB.

Resonance Shift

Work in literature [4, 26] has shown that high optical intensities can result in bi-stability in a variety of in-waveguide configurations from Bragg gratings [27] to ring resonator devices [5]. Unlike in Si where competing effects contribute, the well-documented negligible nature of TPA [17, 22] in silicon-rich nitride films at C-band allows measurements of optical shift to be attributed to temperature changes through the thermo-optic effect driven by linear absorption of a portion of the cavity intensity. The absorption coefficient induced by TPA is linearly dependent on the intensity while the resonant wavelength shift, as shown in equation (1) is dependent on the product of the absorption coefficient and the intensity in the steady state, resulting in a nonlinear relation between the TPA coefficient and resonant wavelength shift in its general form. As such the absorption which results in resonance shift seen here can be attributed to the linear absorption term which is a combination of various forms of absorption including material as well as interface state absorption, determining the exact contributions from each possible effect being beyond the scope

of this work. Regardless, in a ring resonator device on-resonance light is coupled into the cavity where absorption induced heating increases the temperature of the ring causing a resonance shift due to the thermo-optic effect. In this section below we will compare measurements from optically induced resonant shifts to that of thermally heating the chip using a thermo-electric cooler (TEC). First, we demonstrate how this effect can induce a resonant wavelength shift in a ring resonator as a function of input optical power and creates an asymmetry in the line-shape of the resonator. Figure 10 below shows the transmission spectra of the 45um SRN ring resonator device as a function of input optical power.

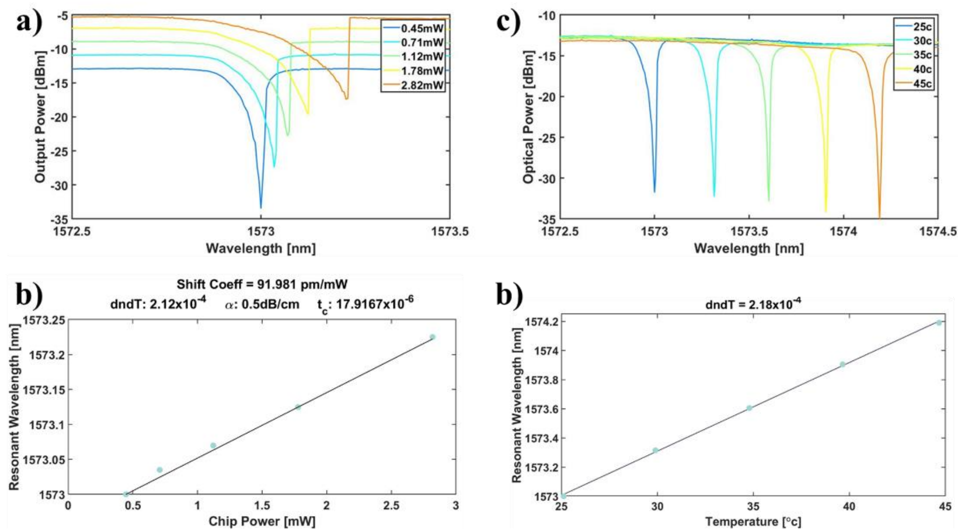

Figure 10: (a) Transmission spectra of a 45um SRN ring resonator for the corresponding on-chip powers in (b). Notice how at the lowest laser power presented the asymmetry is reduced and as the laser power increases the resonant wavelength red-shifts and the resonance becomes increasingly asymmetric. (b) Measured resonant wavelength vs chip power in mW along with a fit line showing a shift coefficient of 91.98 pm/mW for a loss coefficient of 0.5dB/cm. (c) Transmission spectra of a 45um SRN ring resonator as a function of stage temperature from 25∘C to 45∘C. (d) Measured resonant wavelength versus temperature.

Figure 10 shows a measurement of the transmission spectra, sweeping the laser's wavelength at a continuous sweep speed of 5nm/s. From these measurements the resonant wavelength of the ring resonator can be seen to have a linear dependence on the chip power. From

these spectral measurements the shift rate is determined to be 91.98 pm/mW. Following methods laid in [10] by assuming that the absorbed optical intensity in the cavity creates an increase in temperature which shifts the resonant wavelength. Using this method we fit the shift in resonant wavelength vs chip power for the thermo-optic coefficient, absorption coefficient, and the thermal relaxation time. Constraining the absorption coefficient to be less than the measured propagation loss measured in Section 3, as this measured value is a combination of all forms of loss in the ring cavity, we determine the thermo-optic coefficient to be $(2.12 \pm 0.125)\text{x}10^{-4}$ /∘C. It is important to note that due to inherent uncertainties in the absorption coefficient the uncertainty as estimated from the optical shift is larger than that estimated by stage temperature. Second, we measure the transmission spectra as a function of stage temperature, comparing it to the measurement versus chip power. Figure 10(c) shows the measured transmission spectra for stage temperatures from 25∘C to 45∘C. From these measurements the resonant wavelength of the ring resonator can be seen to have a linear dependence on stage temperature from which we can estimate the thermo-optic coefficient to be $(2.18 \pm 0.09)\text{x}10^{-4}$/∘C. Comparing these two measurements of the thermo-optic coefficient we find good agreement in the estimated coefficient. Additionally, it is important to note that it is more challenging to fit for the parameters of interest in the nonlinear regime due to deformation in the resonance and it would be useful for a future work to explore this space further for example as a function of sweep speed of the laser in addition to chip-power.

Time Response

In this section we will measure the temporal response of the self-induce thermo-optic effect in order to demonstrate that it is indeed thermal in nature, as well as estimate the specific thermal relaxation time of our SRN ring resonator device. As we demonstrated in the previous section, the

resonant wavelength of the ring resonator shifts as a function of optical power. In order to measure the temporal response of our device we modulate the intensity of the input optical wave using a pulsed sawtooth wave of increasing frequency in the range of 1kHz to 150kHz, with a delay of 10ms between pulses to allow time for the cavity to relax back to equilibrium. When the wavelength of the laser is fixed at the maxima between resonance positions, the transmitted optical power simply tracks the sawtooth wave of the input, which we refer to as a baseline. Next we set the resonant wavelength detuned by +40pm from the resonant wavelength of the device (1576.6nm). Since increasing optical power during the ramp of the sawtooth causes the filter resonance to red shift past the set laser wavelength, the optical transmission power will show a sudden drop followed by its increase again until the end of the ramp when the output optical power will drop reaching the baseline. After the sawtooth ramp ends and it returns to the initial optical power the resonator returns to equilibrium (i.e., baseline) over a period of thermal relaxation.

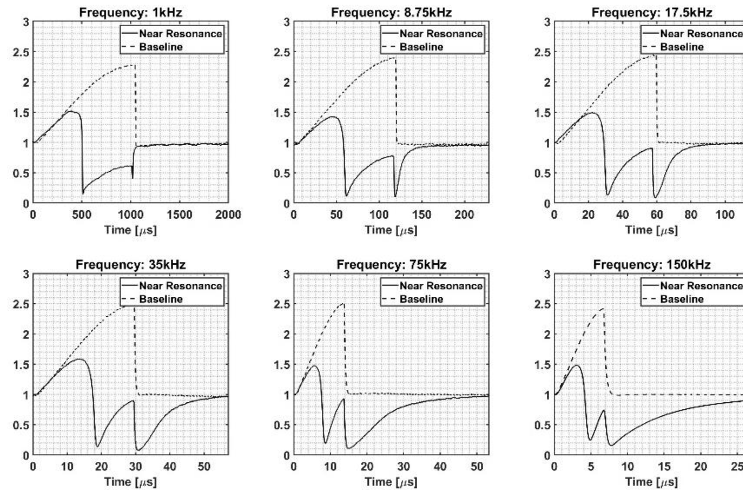

Figure 11: Transmission as a function of time for the 'baseline' curve as well as the 'near resonance' case for ramp 'frequencies' from 1kHz up to 150kHz.

Figure 11 shows a measurement of the transmitted optical power normalized to the transmission at t=0, for the baseline and near resonance case for frequencies from 1kHz to 150kHz

measured using a Hewlett Packard 11982A lightwave converter and a Tektronic TDS3014C digital oscilloscope. As can be observed from Figure 11, at lower frequencies, such as in the 1kHz measurement, there is a sharp drop in the transmitted power around t=500us as expected and then at t=1000us when the sawtooth returns to its initial state there is another sharp drop as the cavity returns to equilibrium. As the frequency of the ramp is increased it becomes clear that after the sawtooth returns to its initial state the cavity requires a relaxation time of ~18.7us to return to equilibrium. If we compare this to the photon lifetime of a 20,000-quality factor ring resonator [25, 28], $\tau_{ph} = \frac{2Q}{\omega_0}$, which is ~33ps we find this clearly indicates our measured relaxation time corresponds to thermal relaxation confirming this as a thermo-optic shift.

Bi-stable Optical Switching

In the previous sections we have demonstrated optically induced thermo-optic shifts in a PECVD SRN ring resonator determining the thermo-optic coefficient to be $(2.12 \pm 0.125)\text{x}10^{-4}/\circ\text{C}$ and the confirmed this to be due to a thermo-optic effect by time response measurements. Finally, in this section we utilize the SRN ring resonator device to demonstrate that the transmitted optical power as a function of input power exhibits a bi-stable regime which is used to demonstrate bi-stable optical switching.

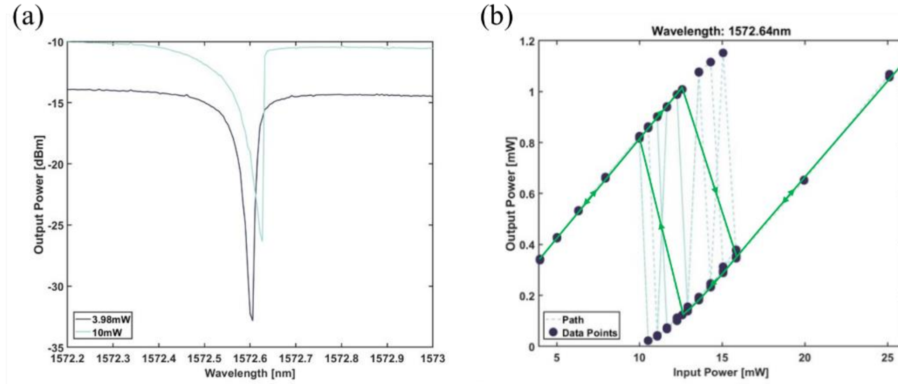

Figure 12: (a) The transmission spectra of the ring resonator device at two different input powers, in black 3.98mW (6dBm), and in teal 10mW (10dBm). Notice how as the input power is increased the resonance becomes more asymmetric and the resonance point red shifts. (b) Transmitted optical power as a function of input optical power demonstrating how there is a region of input power, from approximately 10mW, to 16mW, where multiple solutions are possible. Depending on the way the input power is scanned the transmission can be in either of the branches and be either stable (green loop) or unstable (dashed light-blue lines).

The left-hand plot in figure 12 shows an example of the transmission spectra of the ring resonator device at two different on-chip optical powers, 0.45mW (P_{laser}=6dBm) in black and 1.12mW (P_{laser}=10dBm) in teal. As shown in previous sections, as the input power is increased the resonance becomes more asymmetric and the resonance red shifts. The right-hand plot in Figure 5 is taken by positioning the laser red-shifted from the resonant wavelength at 0.45mW (P_{laser}=6dBm) by +40pm, the transmitted optical power is then measured as a function of input power. The input power is first swept upwards from the minimum power 0.45mW (P_{laser}=6dBm) to the maximum power of 2.8mW (P_{laser}=14dBm), then the input power is swept downwards from 2.8mW (P_{laser}=14dBm) to 1.12mW (P_{laser}=10dBm), after which the input power is linearly looped from 1.12mW (P_{laser}=10dBm) to 1.78mW (P_{laser}=12dBm) to 1.12mW (P_{laser}=10dBm) three times before finally being swept downwards from 1.12mW (P_{laser}=10dBm) to 0.45mW (P_{laser}=6dBm) again. As can be seen by the black connecting lines between the teal datapoints, outside of the 1.12mW to 1.78mW region of on-chip input power the on-chip output power is stable. Inside this

region the power can jump between two bi-stable states. Additionally, if the input power is swept upwards from the below this bi-stable region upwards into it, the output power can be placed in a stable state in the upper branch. If the input power is swept from this state upwards above the maximum of the bi-stable region and then back downwards it can be switched into a stable state in the lower branch. Finally, if the input power is swept downwards from this position below the bi-stable region and then back upwards it can be again placed into a stable state in the upper branch. Using this methodology, we demonstrate bi-stable optical switching, showing a 0,1,0,1,0,1 bit sequence, using a control sequence at the input power. The switching is performed by either 'pulsing' the input power or lower, and then returning the input power to the bias state with a finite ΔP_{in} differential of 0.4dB.

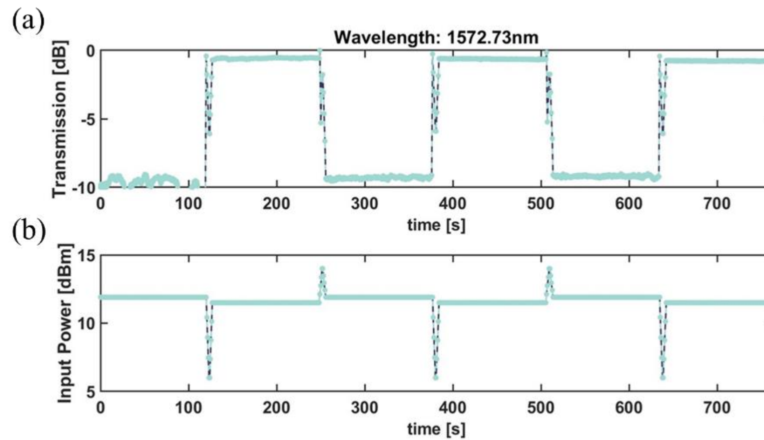

Figure 13: (a) Normalized transmission as a function of time for a '0,1,0,1,0,1' bit sequence. The two stable output states can be switched between using a control sequence on the input power that begins and ends at the same power level with a finite ΔP_{in} differential of 0.4dB. (b) Input power showing the control sequence as well as the ΔP_{in} differential of 0.4dB.

The result of these measurements can be seen in figure 13 as normalized transmission over time for the 0,1,0,1,0,1 bit sequence, where each 'bit' is held for 120s, and each sample point is averaged for 10ms. As the result shows it is possible to stable switch between the two branches shown in Figure 12 using a control sequence and once switched the output is stable in the new state with

10dB of extinction achieved between the two states. Although as we have demonstrated this is a result of the thermo-optic effect, and so speed is limited, it is still a useful demonstration of the ability to cleanly switch between the two bi-stable states and the required input optical power in a high refractive index PECVD SRN all-pass ring resonator and through novel architectures and control schemes such as that in [29, 30] the interplay between this thermally induced effect and the Kerr effect can be explored to develop an ultra-fast bi-stable device.

Conclusion

Optically bi-stable devices are of keen interest for development of optical logic components as well as potentially for other devices such as photonic thermometers [12]. In the past, optical bistability was shown in silicon devices. However, with growing interest in use of silicon nitride devices due to their low loss and negligible TPA, it becomes interesting to explore their ability to realize optical bistability. In recent years it has also been shown that by enhancing the silicon content in silicon nitride films, the second and third order nonlinear susceptibilities as well as the thermo-optic coefficient are increased while maintaining a variety of benefits from stoichiometric silicon nitride, such as the negligible TPA. Despite this however, research into optical bistability and devices design to exploit it have not significantly adopted high silicon content SRN films despite their advantages.

In this manuscript we have presented a study of self-induced thermo-optic bistability in PECVD SRN. We have shown that such PECVD SRN films achieve low propagation loss of 3.07dB/cm and determined the thermo-optic coefficient to be $(2.12 \pm 0.125)\times10^{-4}/\circ C$ by a comparison of optically induced resonance shift and thermal heating. time response measurements were performed which demonstrate a relaxation time of 18.7us at up to 150kHz. Finally, we demonstrated bi-stable optical switching showing that there exists a bi-stable region between

10dBm and 12dBm in which two possible output power states are possible which can be either stable or unstable. PECVD SRN has the potential to enhance optically bi-stable devices by enabling more sensitive temperature sensors due to its enhanced TOC, as well as potentially open new avenues for Kerr based optical bistability if used in an add-drop configuration [11]. In this manuscript we have explored the thermo-optic portion of bistability in PECVD SRN demonstrating it to have significant advantages over stoichiometric nitride based approaches. PECVD SRN is a promising material platform which deserves further research into utilizing it for Kerr based potentially ultrafast bistability and how that interacts with its slower thermo-optic bistability [31].

Acknowledgements

Chapter 2, in part, is a reprint of the material as it appears in Optics Express. The dissertation author was the first author of this paper, with co-authors Dmitrii Belogolovskii, Andrew Grieco, and Yeshaiahu Fainman.

CHAPTER 3 - A SYSTEMATIC EVALUATION OF SILICON-RICH NITRIDE ELECTRO-OPTIC MODULATOR DESIGN AND TRADEOFFS

Introduction

1. Introduction

Optical interconnects form a major part of the disruptive impact of integrated optical systems in a variety of applications, and therefore have driven continued interest in finding the next generation of optical modulators. Historically, high-speed optical modulators have relied upon lithium niobate [1,2] where thanks to the lithium niobate on insulator platform $V_{\pi}L_{\pi}$ metrics on the order of 1.8Vcm have been achieved [3,4], while in search of higher efficiencies other high-k dielectrics have been considered such as barium titanate [5]. All of these materials have three primary challenges:(i) they are in general not CMOS compatible making fabrication more expensive compared to a CMOS process which can be done by a foundry, (ii) they have low refractive indices compared to Silicon requiring larger waveguide cross-sections to achieve mode-confinement, and (iii) they all have higher RF permittivity leading to smaller electric fields in the same cladding at the same applied voltage. As a result many optical interconnects still utilize carrier dispersion in silicon waveguides ($V_{\pi}L_{\pi} \cong 3.5\ Vcm,$ with an insertion loss of 9.2dB) [6], where excess propagation loss due to high dopant concentrations can limit performance, and so there remains interest in a CMOS compatible alternative to such techniques that can disrupt optical modulators in CMOS manufacturing. The issue remains, however, that most CMOS compatible materials either do not exhibit a $\chi^{(2)}$, or exhibit a negligible small one such as lower index silicon nitride films. In recent years work in literature, including past work by the author's [7], has demonstrated that not only can Silicon-rich Nitride (SRN) films exhibit a non-zero $\chi^{(2)}$ but that their refractive index [8, 9], thermo-optic coefficient [10], as well as $\chi^{(2)}$ and $\chi^{(3)}$ [11] are all

enhanced with increasing silicon content which also holds in the case of low temperature plasma-enhanced chemical vapor deposition-based SRN films [8,12]. In this manuscript, we will undertake a systematic evaluation of the contributions from second and third order nonlinear susceptibilities in arbitrary materials and formulate a case for a $\chi^{(3)}$ based linearized electro-optic modulator utilizing a form of heterodyne gain. We will then conduct a numerical study of such a modulator, designing phase-type modulator based on our past works SRN film properties, achieving $V_{\pi}L_{\pi}$ metrics from 1 to 2Vcm and $V_{\pi}L_{\pi}\alpha$ metrics of 116VdB as a phase modulator, or as low as 1Vcm in a push-pull Mach Zehnder Interferometer intensity modulator. We will then explore the integration of such a phase-shift element into a ring resonator cavity as an intensity modulator demonstrating that with proper cavity design and allowing for a degree of coupling miss-match extinction ratios between 12dB and 20dB are achievable. Finally, we will conclude with some discussion on the inherent tradeoffs with such a design and argue that a linearized $\chi^{(3)}$ based modulator, can serve as a viable CMOS compatible alternative to use materials lacking $\chi^{(2)}$ nonlinearities, and as a pure phase modulator alternative to traditional plasma-dispersion approaches in silicon.

Nonlinear Polarizability Analysis

We begin with a brief analysis of second and third order nonlinear optical effects in nonlinear materials with emphasis on the presence of an applied external electric field. Here we include consideration for effects of higher order nonlinearities, beyond that of $\chi^{(3)}$ alone, as research has shown that most CMOS compatible materials lack a $\chi^{(2)}$ as a result of their crystal symmetry [13-16]. Although this is an abbreviated discussion on the topic, a useful place to start is through the induced polarization which can be written as follows [17]:

$$P(r,t) = \epsilon_0 [\chi^{(1)}E(r,t) + \chi^{(2)}E^2(r,t) + \chi^{(3)}E^3(r,t) + \ldots] \quad (1)$$

In equation 3.1, the $\chi^{(1)}$, $\chi^{(2)}$ and $\chi^{(3)}$ represent the first, second and third order nonlinear susceptibilities respectively, which are treated as tensors of rank two, three, and four, respectively. This is a useful formalism because both modulation and wave mixing are understood as solutions to the nonlinear form of Maxwell's equation [17]. If we allow the total electric field $E(r,t)$to be a sum of an optical wave (E_{ω}) and applied electric field (electro-static E_{dc} and time-varying E_{ac}), we can derive expressions for the contributions to the nonlinear portion of the induced polarization, grouping and simplifying terms based on their contributions. Below in equation 3.2, as an example, we show three first terms of eq. 3.1 expansion, grouped and labeled with various nonlinear effects.

$$\begin{aligned}\bar{P}_{NL} &= \epsilon_0\{\overbrace{\chi^{(2)}[2EE^* + E_{dc}^2]}^{\text{Electrostatic}} + \overbrace{\chi^{(2)}[2E_{dc}Ee^{-j\omega t} + 2E_{dc}E^*e^{j\omega t}]}^{\text{Pockels}} + \overbrace{\chi^{(2)}[E^2e^{-j2\omega t} + E^{*2}e^{j2\omega t}]}^{\text{SHG}} + \overbrace{\chi^{(3)}[E_{dc}^3 + 6EE^*E_{dc}]}^{\text{Electrostatic}} \\ &+ \underbrace{\chi^{(3)}[(3E_{dc}^2E + 3E^2E^*)e^{-j\omega t} + (3E_{dc}^2E^* + 3EE^{*2})e^{j\omega t}]}_{\text{Kerr effect and DC-Induced Pockels}} + \underbrace{\chi^{(3)}[3E_{dc}E^2e^{-j2\omega t} + 3E_{dc}E^{*2}e^{j2\omega t}]}_{\text{EFISHG}} + \underbrace{\chi^{(3)}[E^3e^{-j3\omega t} + E^{*3}e^{j3\omega t}]}_{\text{THG}}\}\end{aligned} \tag{3.2}$$

This represents a subset of the possible terms in the nonlinear polarizability, due to our specific choice of terms in the total electric field and additionally the tensorial notation has been suppressed here for simplicity. The terms present in this expansion relate to the various forms of nonlinear processes that utilize the susceptibility as summarized in Table 1. Table 1 shows a breakdown of the terms of the nonlinear polarization based on the combination of optical wave and applied field present in the induced polarization. The items in this table can be thought of as falling into one of two different categories: (1) Effects at the fundamental optical frequency – Switching and modulation and (2) Effects at harmonic frequencies (including 0 frequency) – wave mixing. Switching and Modulation based on the nonlinear susceptibility is typically thought to comprise of the Pockels effect and the Quadratic Electro-optic effect, sometimes called the DC-Kerr effect, where-as wave mixing comprises three and four wave mixing, active and passive. However, terms such as the "EFI-SHG" (here EFI stands for electric field induced) and

“Modulated SHG” blur this distinction and can allow methods for both enhancing second order processes as well as analyzing third order nonlinearities via four-wave mixing. Importantly, if we allow for a combination of electro-static E_{dc} and time-varying E_{ac} together with the optical E_{ω}, we can derive a term (last column in table 1) which allows for third order nonlinearity based linear

Table 1: A breakdown of the induced polarization.

- $\chi^{(1)}$
- $\chi^{(2)}$
- $\chi^{(3)}$
- $\chi^{(4)}$

		Applied Field			
		0	**E^{dc}**	**E^{ac}**	**$E^{ac}E^{dc}$**
Optical Wave	**0**	$\chi^{(2)}$ Optical rectification	$\chi^{(3)}$ Optical rectification		
	ω	Fundamental Wave	Pockels Effect		DC-Induced Pockels Effect
	2ω	SHG	EFI-SHG	Modulated SHG	
	3ω	THG	$\chi^{(4)}$ Effects		$\ddots$

modulation. This is especially interesting to explore, as unlike $\chi^{(2)}$ which is dependent on crystal structure, $\chi^{(3)}$ is present in all materials. In the remainder of this manuscript we will only consider non-resonant electronic nonlinearities as this type of nonlinearity can respond at ultra-fast speeds and is thus of interest for high-speed modulation and switching, as well as be useful for wave-mixing applications [18]. In the following we consider the case of a material which has both $\chi^{(2)}$ and $\chi^{(3)}$ tensors susceptibities (e.g. SRN), in the presence of an applied electric field which has both an electro-static (Edc) and a time-varying ac (Eac) component. From this we derive an expression for each combination to the change in refractive index showing them below in table 2 based on $\chi^{(2)}$ vs $\chi^{(3)}$ and their combination in response to the applied Edc and Eac fields.

Table 2: Second and Third order contributions to the change in refractive index

	DC	AC	AC+DC
$\chi^{(2)}$	$\Delta \mathrm{n}_{dc}^{\chi^{(2)}} = \sum_{jk} \frac{\chi_{ijk}^{(2)}}{n_k^{eq}} E_j^{dc}$	$\Delta \mathrm{n}_{ac}^{\chi^{(2)}} = \sum_{jk} \frac{\chi_{ijk}^{(2)}}{n_k^{eq}} E_j^{ac}$	Not Applicable
$\chi^{(3)}$	$\Delta \mathrm{n}_{dc}^{\chi^{(3)}} = \sum_{jk} \frac{3\chi_{ijjk}^{(3)}}{2n_k^{eq}} E_j^{dc^2}$	$\Delta \mathrm{n}_{ac}^{\chi^{(3)}} = \sum_{jk} \frac{3\chi_{ijjk}^{(3)}}{2n_k^{eq}} E_j^{ac^2}$	$\Delta \mathrm{n}_{ac+dc}^{\chi^{(3)}} = \sum_{jk} \frac{3\chi_{ijjk}^{(3)}}{n_k^{eq}} E_j^{ac} E_j^{dc}$

Table 2 reveals a few interesting features of such an arbitrary material. Specifically, for such a material under the presence of an Edc and Eac field there will be of course a static "bias" change in refractive index represented by $\Delta n_{dc} = \Delta \mathrm{n}_{dc}^{\chi^{(2)}} + \Delta \mathrm{n}_{dc}^{\chi^{(3)}}$; however, there will also be a modulated component of the change in refractive index represented by $\Delta n_{ac} = \Delta \mathrm{n}_{ac}^{\chi^{(2)}} + \Delta \mathrm{n}_{ac}^{\chi^{(3)}} + \Delta \mathrm{n}_{ac+dc}^{\chi^{(3)}}$. If we are interested in constructing a linearized modulator utilizing a given materials $\chi^{(3)}$, as well as $\chi^{(2)}$ when the material possesses it, then analysis of the Δn_{ac} term is important. Additionally it should be noticed that the $\Delta \mathrm{n}_{ac+dc}^{\chi^{(3)}}$ mixed term has an extra factor of 2 compared with the non-mixed terms, $\Delta \mathrm{n}_{dc}^{\chi^{(3)}}$ and $\Delta \mathrm{n}_{ac}^{\chi^{(3)}}$. From these expressions and Table 2 the only contributing term that is not linear in Eac is the $\Delta \mathrm{n}_{ac}^{\chi^{(3)}}$ term, which is the reason third order modulation is typically quadratically chirped, a problem for linear modulator design; however, the term $\Delta \mathrm{n}_{ac+dc}^{\chi^{(3)}}$ has two benefits. First, if we require the Edc >> Eac, a condition that will dictate the degree of linearity, then the $\Delta \mathrm{n}_{ac+dc}^{\chi^{(3)}}$ term is approximately linear in Eac, and additionally under such a condition it is naturally true that $\Delta \mathrm{n}_{ac}^{\chi^{(3)}} \ll \Delta \mathrm{n}_{ac+dc}^{\chi^{(3)}}$ which allows us to ignore the quadratically chirped term. Secondly, the $\Delta \mathrm{n}_{ac+dc}^{\chi^{(3)}}$ term exhibits a natural form of what can be thought of as a heterodyne gain. This term has a weak high-frequency field (Eac) and a strong low-

frequency field (Edc) the product of which produce an effect at the high-frequency field's enhanced by the strength of the low-frequency field (Edc). While this will require the Edc field strength to be high, it will allow the Eac field strength to be proportionally lower, this can be a solution of interest in the CMOS case as 10's of volts-dc can be acceptable whereas the AC voltage is the one that needs to be as low as possible, even sub 1V in some cases. Figure 14 shows an example of how by controlling the ratio of Eac to Edc the quadratic chirping in the resulting change in phase can by removed. Note that as the Eac/Edc ratio increases so does the peak phase change because the magnitude of Eac increases.

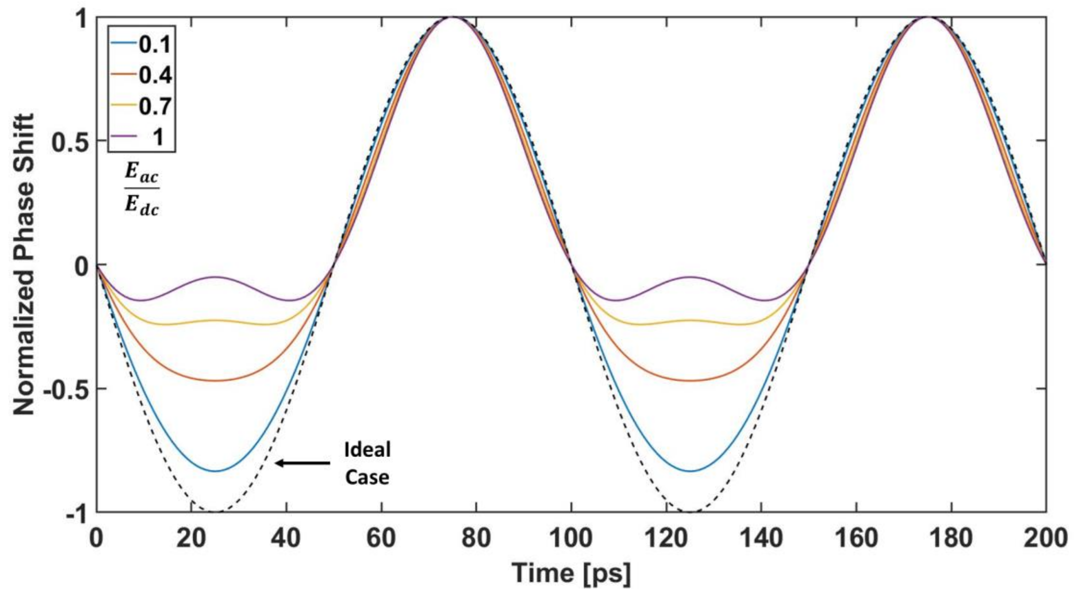

Figure 14: An example for a 10Ghz modulated Eac wave as a function of the fraction of Eac/Edc for a fixed Edc of $1.22\text{x}10^8$ V/m. In the above plot the black dashed line represents the idealized case.

It is important to discuss the trade-off between $\chi^{(2)}$ based Pockels modulation and this $\chi^{(3)}$ based DC-Induced Kerr modulation. As has been derived previously in the literature there is a general rule that the order of magnitude of $\chi^{(2)}$ and $\chi^{(3)}$ should be expected to be $\frac{\chi^{(1)}}{E_{at}}$ and $\frac{\chi^{(1)}}{E_{at}^2}$

respectively [17], where E_{at} is the atomic electric field strength. This has the important implication that we should expect effects based on $\chi^{(3)}$ to be weaker than those of $\chi^{(2)}$ because the order of magnitude of their coefficients in general differ by the atomic electric field strength and thus an effective $\chi^{(2)}$ induced by the presence of an applied dc electric field could only approach that of the expected inherent $\chi^{(2)}$ when the applied electric field approaches that of E_{at}, in materials whose $\chi^{(2)}$ originates from a crystal lattice dipole. Such a condition is of course not possible as the breakdown field of a given material will in general be much lower than E_{at} meaning that we will reach the maximum strength of applied electric field before the combination of $\chi^{(3)}E_{applied}$ is expected to be of the order of the inherent $\chi^{(2)}$. While this may indeed be a limitation, in realistic materials, especially CMOS compatible materials, the $\chi^{(2)}$ tensor is often zero due to crystal symmetry, in such cases this technique can still be useful as all materials have a non-zero $\chi^{(3)}$ tensor. In SRN specifically the approach of combining $\chi^{(2)}$ and $\chi^{(3)}$ becomes very interesting because the exact origin of the non-zero $\chi^{(2)}$ in silicon-rich nitride is still not well understood. As a result this general rule may not hold true for such a material, and consequently the general rule for their ratio to be Eat may not apply. For example, if we define $\chi^{(2)}_{eff} = 3\chi^{(3)}E_{dc}$ and consider our previous results in [7] then we find that at Edc = $1\text{x}10^8$ V/m we have a $\chi^{(2)}_{eff}$ of 180 pm/V compared to the measured 14 pm/V inherent $\chi^{(2)}$ which indicates that for SRN a value of $\chi^{(2)}_{eff} > \chi^{(2)}$ is possible. For this reason, we will explore the design of a linearized modulator based on the DC-Induced Kerr effect in SRN. It has been shown in literature in past work by the author [7] as well as others [11] that PECVD SRN can exhibit refractive indices as high as 3.1 and has a comparably enhanced $\chi^{(3)}$. Additionally, silicon-rich nitride films are expected to have a high breakdown field as well as low optical loss over a broader spectral range that Silicon [9, 11, 19].

As the example calculation of a $\chi_{eff}^{(2)}$ shows, these unique properties can make SRN films very attractive for CMOS manufacturing.

Phase Modulator Design

We begin by analyzing a fundamental building block such as a phase shifter element on its own. Figure 15(a) shows a schematic cross-section of the proposed device structure. In the structure an SRN waveguide is located on a SiO_2 buried oxide layer. We then create a conformal thin dielectric shield layer (e.g., deposited using ALD) followed by construction of gold (Au) electrodes. Finally, the structure has a top cladding layer of SiO_2. This structure can be thought of as the generic case of a device which lacks such a shield layer, the case where the shield dielectric is SiO_2 and a case where the left and right electrodes could also be placed directly onto the bottom SiO_2 layer and then the center electrode formed after depositing a desired thickness of SiO_2. We consider the presented generic device in Fig. 2a as a useful layout for discussing important tradeoffs of such designs. Firstly, the objective is to maximize the strength of the applied electric field within the waveguide core while minimizing the induced optical loss, a trade-off which will dictate the optimal device performance regime. One key parameter that will dictate the strength of the applied field is the ratio of the relative permittivity of the shield layer to that of the SRN waveguide layer.

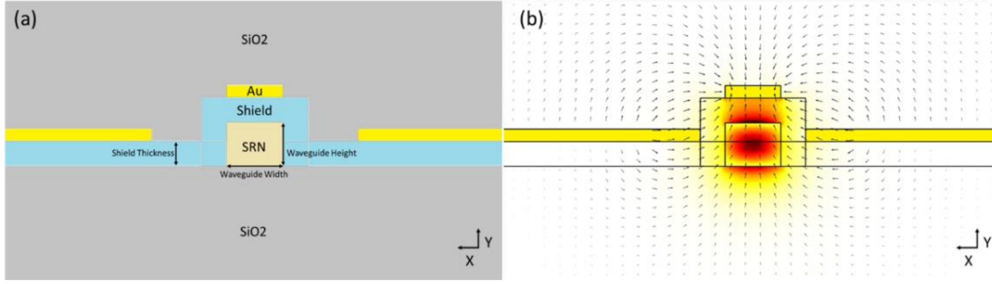

Figure 15: (a) Schematic cross-section of the proposed device structure. A Silicon-rich Nitride waveguide sits on a SiO2 buried oxide layer. On top of the Silicon-rich Nitride waveguide is a thin dielectric shield layer onto which Ground-Signal-Ground gold electrodes are formed. Finally, the top of the structure is top clad with SiO2. (b) Image showing the TM optical mode for a 350nm thick, 450nm wide SRN waveguide along with field lines for an applied electric field from the Ground-Signal-Ground (GSG) field lines.

Therefore, if we utilize a thin cladding layer of low refractive index silicon nitride, which is known to have an RF permittivity around 7.2 [20], to more closely match the RF permittivity of the interface to that of the SRN waveguide core which we have previously measured to be 9.44 [7], we can increase the penetration of the applied electric field into the waveguide. However, the trade-off is that utilizing a silicon nitride shield layer will reduce the refractive index contrast of the waveguide core, reducing mode confinement and thus increasing induced optical loss due to the proximity of the electrodes.

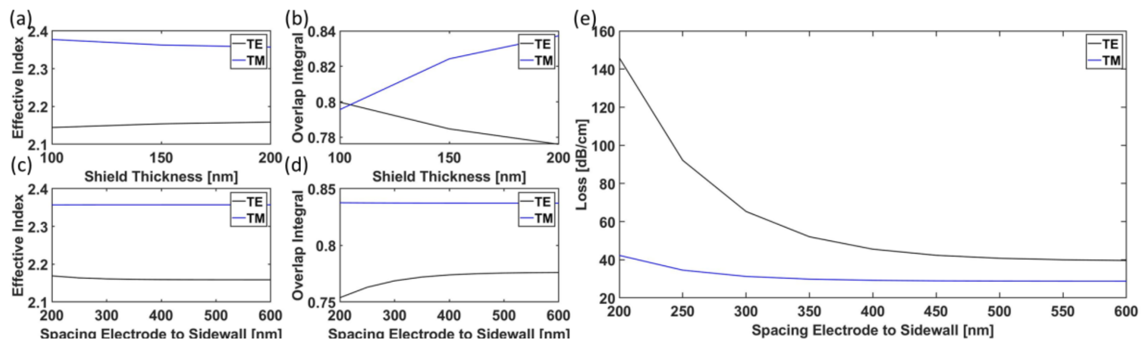

Figure 16: (a) Effective Index of the TE-like and TM-like modes vs SiO2 'shield' thickness. (b) Overlap Integral of the TE-like and TM-like modes with the SRN waveguide core versus SiO2 'shield' thickness. (c) Effective Index of the TE-like and TM-like modes vs spacing from the electrode to waveguide sidewall. (d) Overlap Integral of the TE-like and TM-like modes with the SRN waveguide core versus

spacing from the electrode to waveguide sidewall. (e) Propagation Loss vs electrode to sidewall spacing for the TE-like and TM-like modes.

In general the use of an intermediate dielectric shield layer between the waveguide core and the metal electrodes is a necessity due to optical losses from metals; however, once introduced the mismatch in RF permittivity between the intermediate dielectric shield layer and the waveguide core will “shield” the higher RF permittivity waveguide core from the applied electric fields reducing the strength of the field within the nonlinear medium. The solution then is to utilize a material which matches the RF permittivity of the silicon-rich nitride core; however, when considering practical materials often the RF permittivity and the refractive index increase in tandem. For example, at ~7.2 silicon-nitride [20] has an expected RF permittivity closer to that of SRN however it has a higher refractive index of 1.8 to 1.95 compared to the 1.45 of SiO_2 which has an RF permittivity in the range of 3.75 to 4.45 [21, 22]. The result of this is that in a realistic CMOS compatible material stack with limited choices for dielectric shield layers there is a tradeoff between the strength of the applied electric field and the loss of the optical mode from the lower modal confinement of a higher refractive index cladding layer. In the design of the phase shift element in this study we will use SiO_2 as the shield layer in order to mitigate excess loss from modal deconfinement. This means that since the shield layer is the same material as the cladding it serves as a physical spacer rather than any additional RF permittivity matching. Our proposed structure will be based on the expected $\chi^{(2)}$ and $\chi^{(3)}$ values for silicon-rich nitride films of similar refractive index in literature such as 14 pm/V and $6x10^{-19}$ m^2/v^2 from our past work [7] with a good review in [23]; we will utilize the measured RF permittivity from that work as well [7]. Figure 15(b) shows a COMSOL model of the TM optical mode for a 350nm thick 450nm wide Silicon-rich Nitride waveguide along with the applied electric field lines from the ground-signal-ground (GSG) electrodes. Utilizing COMSOL and Lumerical we simulate the electrical and optical fields

of the structure as a function of both the electrode to waveguide sidewall spacing as well as the thickness of the shield layer and optimize the width and height of the waveguide to minimize excess at 500nm thick and 350nm wide and assume a SiO_2 shield layer. As in this case the shield layer is assumed to be the same as the cladding, it serves simply as a physical spacer rather than as both a physical spacer and permittivity matching. For these simulations as outlined in section 2, we will consider the case where the mean value of E_{dc} in the core is as large as $1.22x10^8$ V/m at peak value, taking results from COMSOL simulations.

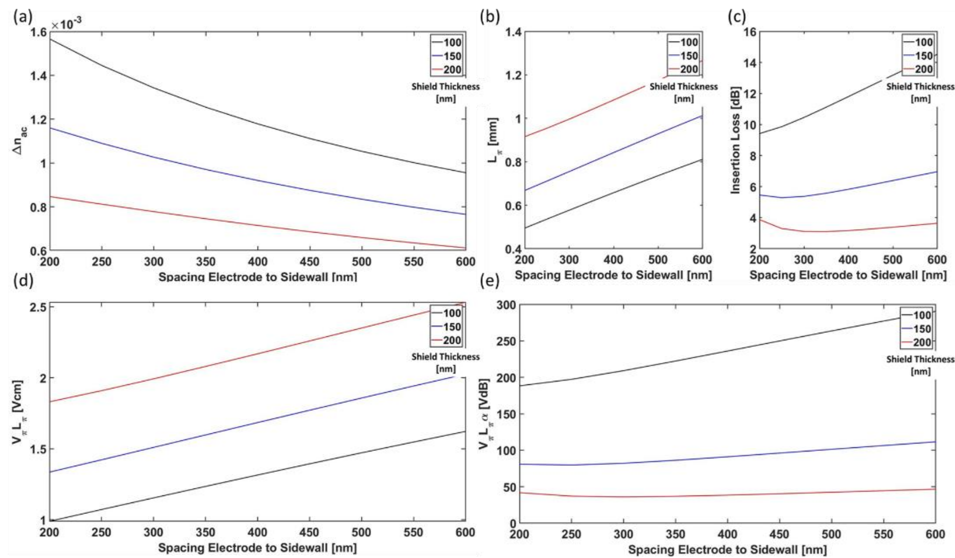

Figure 17: (a) A plot of the change in refractive index under the presence of a combination of AC and DC field. In such a situation if we require that Edc >> Eac then we can write this as approximately $\Delta n_{ac} = \Delta n_{ac}^{\chi^{(2)}} + \Delta n_{ac+dc}^{\chi^{(3)}}$. (b) A plot of the require length for a π phase shift based on Δn_{ac} as a function of electrode to sidewall spacing and shield thickness. (c) A plot of lumped loss for a phase shifter with a length of L_{π} as a function of electrode to sidewall spacing and shield thickness. (d) From the change in refractive index we can determine the metric $V_{\pi}L_{\pi}$. (e) While the metric $V_{\pi}L_{\pi}$ is a commonly used metric for such devices, a more comprehensive metric is $V_{\pi}L_{\pi}\alpha$ which includes loss and is thus in units of V-dB instead of V-cm.

Figure 16(a-b) shows the effective index and overlap integral of the TE-like and TM-like modes as a function of shield thickness. In the case where the shield is simply the same as the cladding it serves as a physical spacer predominately for the central electrode. As a result, at small

shield thickness the TM-like optical mode gets pulled into the thin gap between the center electrode and the waveguide core, increasing the effective index but decreasing the overlap with the SRN layer. In figure 16(c-d) a similar effect occurs for the TE-like mode when the electrodes are brought closer to the sidewall of the waveguide with the enhancement of the effective index, and corresponding decrease in overlap integral, being smaller due to large gaps than the shield layer thickness for the TM-like mode. The tradeoff of course is loss, which is shown in Figure 16(e): when the electrode to sidewall spacing is reduced the loss increases. Naturally, the TE-like mode experiences a faster increase in loss from bringing the electrodes closer to the side-wall were as the TM-like case will see a faster increase as the shield thickness decreases. It is important to revisit and note tensorial nature of $\chi^{(2)}$ and $\chi^{(3)}$ in light of these TE- and TM- like mode polarizations. Specifically, the different tensor components are utilized depending on the orientation of the optical mode polarization and the direction of the applied electric fields. As discussed in section 2, the fundamental relation between second and third order nonlinearities, and the presences of a non-zero $\chi^{(2)}$ in SRN, means that all else being equal a TM polarized optical mode and vertically applied electric field will couple to the largest nonlinear susceptibility $\chi^{(2)}$ and $\chi^{(3)}$ tensor components and consequently, produce the largest change in refractive index. As such in this manuscript we will focus on the case utilizing the $\chi^{(3)}_{3333}$ tensor component which maximized the interaction between the TM-like optical mode and vertical applied electric fields. Note, however, that a variety of other configurations could be explored in the future such as combinations which use not-colinear tensor components for example an in-plane applied field and a TM-like optical mode. Next, we investigate a specific design for TM-like mode phase modulation using a device with electrode to sidewall spacings varying from 200nm to 600nm and shield thickness varying from 100nm to 200nm. Fig. 17(a) shows the predicted Δn_{ac} for these

geometries for the case of applied voltages Vac and Vdc, 20v and 200v respectively. The trade-off here is that at a fixed voltage smaller electrode to sidewall spacings result in larger applied field strengths at a fixed voltage, and thus larger changes in refractive index. Similarly, decreasing the shield layer thickness increases the applied field strength in the waveguide core at a fixed voltage and thus increases the change in refractive index. From the change in refractive index curves the minimum length required for a π phase shift (L_π) is determined as a function of electrode to sidewall spacing and shield thickness in figure 17(b). As the shield thickness increases the strength of the applied electric field in the waveguide core reduces thus requiring longer path lengths to maintain a π phase shift. Using the lengths from figure 17(b) and the propagation loss values discussed in figure 16(e) we generate predicted values for the insertion loss in figure 17(c) reaching values as low as 3.1dB. Figure 17(d) then, shows the predicted $V_\pi L_\pi$ for each corresponding design case under the condition that $\frac{E_{dc}}{E_{ac}} \cong 10$. From this it is clear that we can achieve competitive $V_\pi L_\pi$ metrics, from 1 to 1.8Vcm. However, this is only a part of the story as a comprehensive figure of merit should include the loss, so we define an additional figure of merit to be $V_\pi L_\pi \alpha$ which results in a unit of VdB. Figure 17(e) shows such a figure of merit including the loss in the analysis. The way to interpret such a figure of merit is to consider that at a $V_\pi L_\pi \alpha$ of 37 VdB a 20Vpp AC voltage would have an insertion loss of 1.85dB. It is through a combination of these two figures of merit that the design space, and tradeoffs between voltage, length, and insertion loss can be understood. Based on these results then the following performance can be achieved for such a SRN Modulator.

Table 3: Example Possible Design Parameters

Vdc [V]	Vac [Vpp]	L [mm]	IL [dB]
-200	-20	1	3.1
-200	-6.2	3.2	10

Table 3 shows the expected performance for our considered design. A clear trend in this design then is a tradeoff between voltage and lumped loss, for example at a $V_{\pi}L_{\pi}$ of 2Vcm with a 6.2Vpp ac voltage we get 10dB or at 20Vpp we get 3.1dB. On the other hand we can achieve the minimum 1Vcm $V_{\pi}L_{\pi}$ metric at an insertion loss of 9.4dB.

Intensity Modulator Design

In the previous section we discussed the design and performance of a phase modulator, which provides important insight into the fundamental performance of the underlying device. We will next discuss how such a phase shift element can be used as an intensity modulator by embedding it into a ring resonator cavity or in a Mach Zehnder interferometer (MZI) configuration. Both ring-resonator and MZI configurations have their own advantages and drawbacks which we will discuss but they can be thought of as broadly representing the two categories of intensity modulators, resonant and non-resonant respectively. As has been well reported in literature [24, 25] a ring resonator can be viewed as a form of a resonant filter, which when the resonant condition, $\phi_{roundtrip} = m2\pi$, is satisfied light is lost from the transmission port while off resonant light is allowed to pass. It is this condition that allows a phase-modulator embedded into the cavity of a ring resonator to be realized as an intensity modulator, the phase introduced by the phase modulator adds to the nominal roundtrip phase and changes the wavelength at which the nominal

round trip phase plus the phase change from the modulator results in an integer multiple of 2π. The well-known expression for the transmission (T_p) from an all-pass ring resonator is given by:

$$T_p = \frac{a^2 - 2racos(\phi) + r^2}{1 - 2arcos(\phi) + (ra)^2} \quad (3)$$

Where r is the self-coupling coefficient of the bus waveguide, k is the cross-coupling coefficient, a is the single-pass amplitude transmission, and ϕ is the single-pass phase shift. In the idealized case the critical coupling condition can be shown to be when the coupled power is equal to the power lost in the ring, or $r = a$. In figure 18 below we consider embedding the phase-shift element from section 3 into a $45\mu m$ bend radius ring resonator made of SRN. Additionally, we consider the case where there is an unintende' mismatch between the amplitude transmission coefficient and the self-coupling coefficient of 0.05, as a typical value to account for fabrication and design variation (based on our past experience) and where the phase modulator comprises 90% of the cavity length, to accommodate the coupling region unperturbed by electrodes.

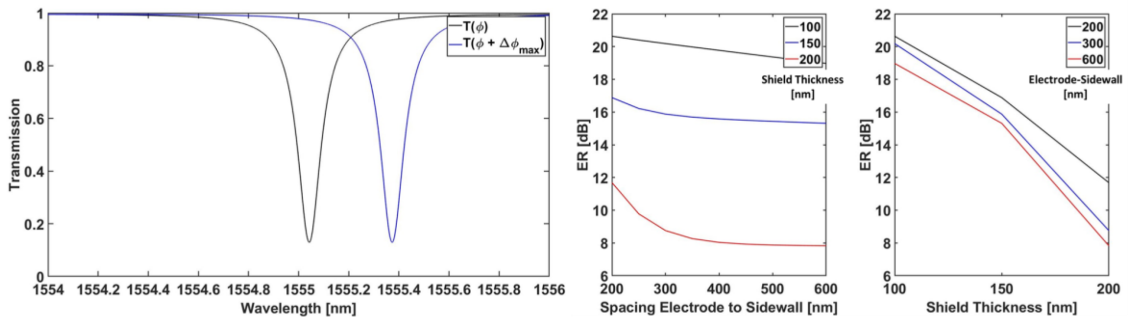

Figure 18: (a) Simulated Transmission spectra and maximum shift in transmission spectra for a 45um bend radius ring modulator assuming a $\Delta_{r-a} = 0.05$ mismatch between the single pass amplitude transmission coefficient and the self-coupling coefficient of the bus. (b) Extinction Ratio as a function of electrode to sidewall spacing for shield thickness 100nm to 200nm. (c) Extinction Ratio as a function of shield thickness for electrode-sidewall spacings from 200nm to 600nm.

Figure 18(a) shows the transmission spectra of the nominal device $T(\phi)$ in black along the expected shifted transmission spectra $T(\phi + \Delta\phi_{max})$ due to modulated amplitude, Δn_{ac}. Figure

18(b) and(c) show the expected extinction ratio (ER), defined as the ratio $T(\phi + \Delta\phi_{max})/T(\phi)$, as a function of electrode to sidewall spacing and shield thickness respectively. Two general trends can be observed in figure's 18(b) and (c): increasing electrode to sidewall spacing decreases the ER and increasing shield thickness decreases the ER. As long as the ring resonator is in the critical coupling regime, increasing either the electrode to sidewall spacing or the shield thickness reduces the ER by decreasing the strength of the applied field within the waveguide core. On the other hand, as it has been discussed in Section 3, reducing the electrode to sidewall spacing or the shield thickness increases the loss, in the case of a ring resonator this impacts the maximum achievable quality factor. In turn a commonly used definition of the quality factor is the ratio of stored energy in the cavity to energy dissipated per cycle and therefore is a measurement of the rate of decay of energy in the cavity [26]. These two factors form a tradeoff which is visible in Figure 19(a) and (b).

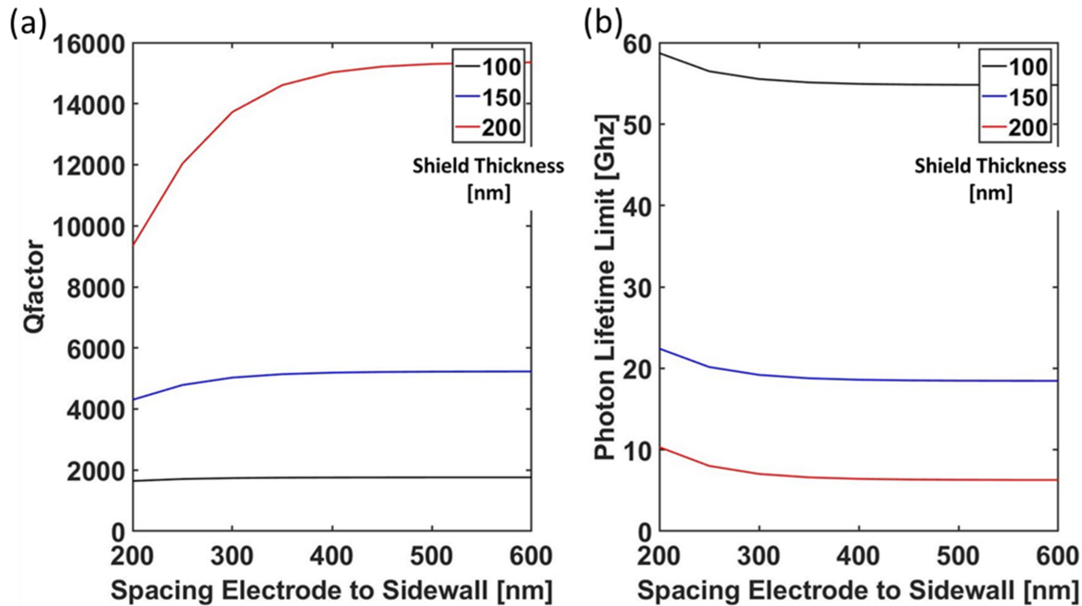

Figure 19: (a) Quality Factor versus electrode to sidewall spacing for shield thickness 100nm to 200nm (b) Photon lifetime limited bandwidth vs electrode to sidewall spacing for shield thickness 100nm to 200nm.

Figure 19(a) shows the expected quality factor of a ring resonator with a Δ_{r-a} mismatch of 0.05 vs electrode to sidewall spacings for shield thickness from 100nm to 200nm. As mentioned above, the reduction in quality factor for increasing loss (decreased electrode to sidewall spacing or decreased shield thickness) can clearly be observed. As ring resonators are resonant cavities the enhanced intensity contrast is a tradeoff with the ring-down time of the cavity which limits response times. Using the quality factor vs electrode to sidewall spacing and shield thickness we present the photon-lifetime limited bandwidth, $\frac{1}{2\pi\tau_{cavity}}$, where τ_{cavity} is the photon lifetime of the cavity and related to the quality factor as $Q = \frac{\omega_0\tau_{cavity}}{2}$ [26, 27]. From figure 19(b) we observe that increasing quality factor's results in lower photon lifetime limited bandwidths, reaching as low as ~10Ghz for the largest quality factors. Additionally, there is a slight enhancement in photon lifetime limited bandwidth at the smallest electrode to side wall spacings. Based on these results a photon lifetime limit of 60Ghz requires a quality factor of 2000, which is naturally achieved at a shield thickness of 100nm. Therefore, integrating our phase modulator into a ring resonator cavity will allow ER's of 10dB to 20dB and photon lifetime bandwidths of 60Ghz for Q factors of 2000. We will next discuss the MZI configuration as a non-resonant alternative for intensity modulation. Unlike the ring resonator, the MZI configuration being non-resonant does not have a photon lifetime limit to its bandwidth instead it is limited by the capacitive load of the electrodes. Here we consider an unbalanced MZI, with a mismatch length of 200μm, and the phase modulator of length L_π from Section 3 in both arms. Figure 20(a) shows the simulated spectral response of such an unbalanced MZI in the nominal case $T(\phi)$.

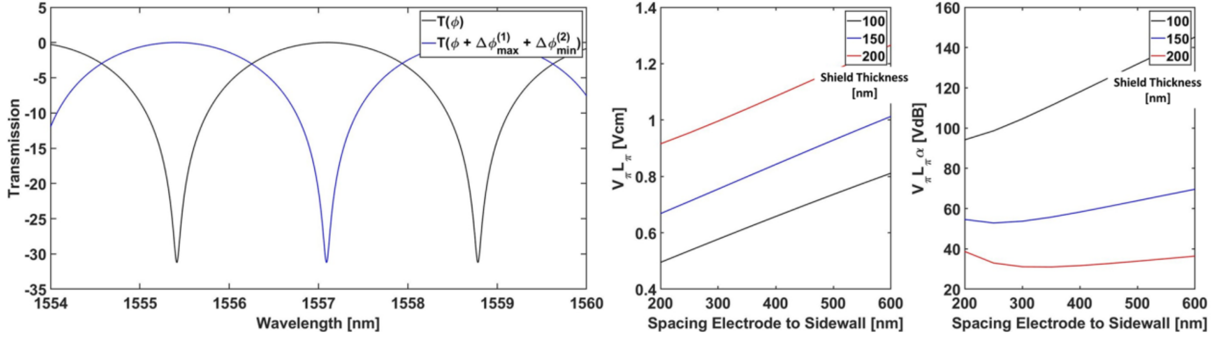

Figure 20: (a) Simulated Transmission spectra and maximum shift in transmission spectra for a MZI with an imbalance length of 200μm along with electrodes of the L_π length from section 3 in both arms driven in push-pull. (b) A plot of the $V_\pi L_\pi$ metric versus electrode to sidewall spacing and shield thickness. (c) A plot of the $V_\pi L_\pi \alpha$ metric versus electrode to sidewall spacing and shield thickness.

In the case of the MZI by controlling the relative phases introduced into both arms we can form an intensity modulator. In this case we will consider the push-pull configuration where the electrical driving signal of the two arms is π out of phase with each other. The resulting $V_\pi L_\pi$ and $V_\pi L_\pi \alpha$ metrics are shown in figures 20(b) and (c) respectively. The analysis here is a fairly straightforward extension of the phase modulator, as figure 20(a) shows a full π phase shift in the spectra is achievable and the corresponding figures of merit clarify that the in addition to converting the phase modulator into an intensity modulator, we have cut the $V_\pi L_\pi$ in half, achieving values of 0.5Vcm to 0.9Vcm as a result of utilizing pushpull operation. The primary trade-offs in such an MZI design are primarily ones of compactness and are discussed next. Unlike the ring resonator configuration which can be made as small as twice the bend radius of choice, the MZI here requires electrode lengths of L_π which is 1mm, or longer. The trade-off here then is that we cut the $V_\pi L_\pi$ metric down as low as 0.5Vcm in the push-pull MZI but the longer electrode's relative to these in the ring resonator as well as being driven in push-pull mode, will likely to lead to a parallel set of capacitances, relative to the phase modulator. This leads the MZI configuration to have the largest capacitance of the three configurations discussed. For example, if we compare our

results to literature, such as that of lithium niobate on insulator devices [3], we find that SRN Mach Zehnder can achieve a $V_\pi L_\pi$ between 0.5 to 0.9Vcm while lithium niobate on insulator devices achieves values in the range 1.8Vcm; however, if we compare to only CMOS compatible techniques such as a depletion type silicon modulator [6] we find values in the range of 3.5Vcm. In table 4 below we have summarized a comparison of various modulator platforms from literature.

Table 4: A comparison of Modulator Performance

	$V_\pi L_\pi$ [Vcm]	IL [dB]	RF Permittivity	Bandwidth	CMOS	Reference
This work	1	1.55	9.45	20 to 60Ghz	*yes*	-
Depletion type Silicon	3.5	9.2	N/A	~20Ghz	yes	[6]
Lithium Niobate on Insulator	1.8	2	28	~ 15 Ghz	no	[3]
Hybrid Lithium Niobate on Silicon	2.7	1.8	not stated	> 70 Ghz	no	[4]
Silicon on BTO thin-film	0.23	not stated	100 - 3000	~20 Ghz	no	[5]

These techniques range from lithium niobate on insulator to hybrid Silicon on barium titanate (BTO) thin-film approaches. Of these various approaches the silicon on BTO thin-film achieves the clear best $V_\pi L_\pi$ metric; however, being a silicon on BTO thin-film device requires post-processing and is not in general CMOS compatible. Additionally, the large nonlinearities that allow for low voltage's are in general smaller when used for wave-mixing. Of the approaches in the table, our result and the depletion type silicon modulator are the only two that can be clearly defined as CMOS compatible material stacks. Our numerical study shows that SRN DC-Induced Kerr modulators can achieve competitive $V_\pi L_\pi$ metrics and being a low temperature PECVD process it can bring new capabilities to CMOS compatible platforms.

Discussion and Conclusion

Traditionally electro-optic modulators have relied upon second order nonlinearities, utilizing the Pockels effect; however, materials that exhibit non-zero $\chi^{(2)}$ tensors are generally not CMOS compatible. Meanwhile $\chi^{(3)}$ based modulation has typically been seen as un-attractive due to a much weaker nonlinearity exhibited by most materials as well as the quadratic nature of the effect. In this manuscript we have undertaken a systematic evaluation of electro-optic nonlinearities in a generic material and then made the case that the unique combination of $\chi^{(2)}$ and $\chi^{(3)}$ exhibited by SRN makes it a good candidate for capacitive $\chi^{(3)}$ based electro-optic modulation. We have shown that SRN can achieve $V_{\pi}L_{\pi}$ metrics as low as 1Vcm in a MZI configuration and extinction ratios as high as 18dB in a ring resonator configuration all utilizing a CMOS compatible material platform. Additionally, we addressed the traditional drawback of quadratic chirping in $\chi^{(3)}$ based modulators by showing that the superposition (Eac + Edc) and proper choice of the Eac/Edc ratio can not only linearize the change in optical carrier phase but can also be seen as a heterodyne gain amplification of a weak Eac field by a large Edc field. While for some applications utilizing a non-CMOS device such as a lithium niobate on insulator modulator can be acceptable, there is a need for CMOS compatible alternatives to such devices. As it stands now if a designer is limited to CMOS processing due to a desire to utilize cost effective tape outs then they are primarily limited to carrier dispersion-based modulators in silicon. In this manuscript we have argued that adoption of a $\chi^{(3)}$ based modulator can provide additional utility to such CMOS platforms and that SRN is a good candidate for such adoption. PECVD based silicon nitride films are already widely utilized in CMOS tape outs, and as has been shown in the past by the authors [7, 8], with proper tuning of gas flow ratios a high refractive index PECVD

SRN film can be achieved under otherwise the same processing conditions. In this manuscript we have shown that the unique advantages of high confinement guiding in a low RF permittivity high $\chi^{(3)}$ and low loss in such a platform makes it an attractive candidate for integration into standard CMOS process flows. Further exploration of linearized $\chi^{(3)}$ based modulators in a variety of other CMOS compatible material platforms can provide new and unique capabilities and deserves further investigation.

Acknowledgements

Chapter 3, in part is currently being prepared for submission for publication of the material with co-authors Dmitrii Belogolovskii, Andrew Grieco, and Yeshaiahu Fainman. The dissertation author was the first author of this material.

REFERENCES

Chapter 1

1. C. Wang, M. Zhang, B. Stern, M. Lipson, and M. Loncar, Opt. Exp., 28, 1547 (2018).

2. S. Abel, S. Thilo, C. Marchiori, D. Caimi, L. Czornomaz, M. Stuckelberger, M. Sousa, B. J. Offrein, and J. Fompeyrine, Journal of Lightwave Technology, 34, 1688 (2016).

3. T. Ning, H. Pietarinen, O. Hyvarinen, J. Simonen, G. Genty, and M. Kauranen, Applied Physics Letters, 16, 161902 (2012).

4. K. J. A. Ooi, D. K. T. Ng, T. Wang, A. K. L. Chee, S. K. Ng, Q. Wang, L. K. Ang, A. M. Agarwal, L. C. Kimerling, and D.T.H. Tan, Nature Communications, 8, 13878 (2017).

5. H. Lin, R. Sharma, A. Friedman, B. M. Cromey, F. Vallini, M. W. Puckett, K. Kieu, and Y. Fainman, APL Photonics, 4, 036101 (2019).

6. K. Ikeda, R. E. Saperstein, N, Alic, and Y. Fainman, Opt. Exp. 16, 12987 (2008).

7. E. Timurdogan, C. V. Poulton, M. J. Byrd, and M. R. Watts, Nature Photonics, 11, 200 (2017).

8. M. Nedeljkovic, R. Soref, and G. Z. Mashanovich, IEEE Photonics Journal, 3, 1171 (2011).

9. R. W. Boyd, Nonlinear Optics Third Ed., Elsevier (2003).

10. S. Habermehl, R. T. Apodaca, and R. J. Kaplar, Applied Physics Letters, 4, 012905 (2009).

11. D. K. Ng, Q. Wang, T. Wang, S. Ng, Y. Toh, K. Lim, Y. Yang, and D. T. H. Tan, ACS applied materials & interfaces, 7, 21884 (2015).

12. D. T. H. Tan, K. J. A. Ooi, and D. K. T. Ng, Photonics Research, 6, B50 (2018)

13. H. Nejadriahi, A. Friedman, R. Sharma, S. Pappert, Y. Fainman, and P. Yu, Optics Express, 28, 24951 (2020).

14. S. Habermehl, R.T. Apodaca, and R. J. Kaplar, Applied Physics Letters, 94, 012905 (2009).

15. S. Yoshinaga, Y. Ishikawa, Y. Kawamura, Y. Nakai, Y. Uraoka, Materials Science in Semiconductor Processing, 90, 54 (2019).

16. R. Sharma, M. W. Puckett, H. Lin, A. Isichenko, F. Vallini, and Y. Fainman, Opt. Lett. 41, 1185 (2016).

17. W. Bogaerts, P. D. Heyn, T. V. Vaerenbergh, K. D. Vos, S. K. Selvaraja, T. Claes, P. Dumon, P. Bienstman, D. V. Thourhout, and R. Baets, Laser & Photonics Reviews, 6, 47 (2012).

18. M. W. Puckett, R. Sharma, H. Lin, M. Yang, F. Vallini, and Y. Fainman, Opt. Exp., 24, 16923 (2016).

19. A. Billat, D. Grassani, M. H. Pfeiffer, S. Kharitonov, T. J. Kippenberg, and C. Bres, Nature Communications, 8, 1016 (2017).

20. C. Wu, Y. Lin, S. Su, B. Huang, C. Tsai, H. Wang, Y. Chi, C. Wu, and G. Lin, ACS Photonics, 8, 1141 (2015).

21. G. Lin, S. Su, C. Wu, Y. Lin, B. Huang, H. Wang, C. Tsai, C. Wu, and Y. Chi, Scientific Reports, 5, 9611 (2015).

22. A. Martinez, J. Blasco, P. Sanchis, J. Galan, J Garcia-Ruperez, E. Jordana, P. Guatier et al., Nano letters, 10, 1506 (2010).

23. J. W. Jang, S. J. Chung, W. J. Cho, T. S. Hahn, and S. S. Choi, Journal of Applied Physics, 81, 6322 (1997).

24. C. Lacava, S. Stankovic, A. Z. Khokhar, T. D. Bucio, F. Y. Gardes, G. T. Reed, D. J. Richardson, and P. Petropoulos, Scientific Reports, 7, 22 (2017).

25. K. Luke, Y. Okawachi, M. R. E. Lamont, A. L. Gaeta, and M. Lipson, Opt. Lett. 40, 4823 (2015).

Chapter 2

1. Sethi, Purnima, and Sukhdev Roy. "Ultrafast all-optical flip-flops, simultaneous comparator-decoder and reconfigurable logic unit with silicon microring resonator switches." IEEE Journal of Selected Topics in Quantum Electronics 20.4 (2013): 118-125.

2. Keshtkar, Peyman, Mehdi Miri, and Navid Yasrebi. "Low power, high speed, all-optical logic gates based on optical bistability in graphene-containing compact microdisk resonators." Applied Optics 60.24 (2021): 7234-7242.

3. Nadimi, P., D. D. Caviglia, and E. Di Zitti. "Exploiting silicon-on-insulator microring resonator bistability behavior for all optical set-reset flip-flop." International Journal of Physical and Mathematical Sciences 6.11 (2012): 1485-1489.

4. Almeida, Vilson R., and Michal Lipson. "Optical bistability on a silicon chip." Optics letters 29.20 (2004): 2387-2389.

5. Nikitin, Andrey A., Ilya A. Ryabcev, Aleksei A. Nikitin, Alexandr V. Kondrashov, Alexander A. Semenov, Dmitry A. Konkin, Andrey A. Kokolov, Feodor I. Sheyerman, Leonid I. Babak, and Alexey B. Ustinov. "Optical bistable SOI micro-ring resonators for memory applications." Optics Communications 511 (2022): 127929.

6. Priem, Gino, Pieter Dumon, Walter Bogaerts, Dries Van Thourhout, Geert Morthier, and Roel Baets. "Optical bistability and pulsating behaviour in Silicon-On-Insulator ring resonator structures." Optics express 13, no. 23 (2005): 9623-9628.

7. Rukhlenko, Ivan D., Malin Premaratne, and Govind P. Agrawal. "Analytical study of optical bistability in silicon ring resonators." Optics letters 35.1 (2010): 55-57.

8. Sun, Peng, and Ronald M. Reano. "Low-power optical bistability in a free-standing silicon ring resonator." Optics letters 35.8 (2010): 1124-1126.

9. Chiangga, Surasak, Santhad Pitakwongsaporn, Till D. Frank, and Preecha P. Yupapin. "Optical bistability investigation in a nonlinear silicon microring circuit." Journal of lightwave technology 31, no. 7 (2013): 1101-1105.

10. Ikeda, Kazuhiro, Robert E. Saperstein, Nikola Alic, and Yeshaiahu Fainman. "Thermal and Kerr nonlinear properties of plasma-deposited silicon nitride/silicon dioxide waveguides." Optics express 16, no. 17 (2008): 12987-12994.

11. Yoshiki, Wataru, and Takasumi Tanabe. "Add-drop system for Kerr bistable memory in silicon nitride microrings." arXiv preprint arXiv:1308.6042 (2013).

12. Zhang, Cheng, Guo-Guo Kang, Jin Wang, Shuai Wan, Chun-Hua Dong, Yi-Jie Pan, and Ji-Feng Qu. "Photonic thermometer by silicon nitride microring resonator with milli-kelvin self-heating effect." Measurement 188 (2022): 110494.

13. Friedman, Alex, Hani Nejadriahi, Rajat Sharma, and Yeshaiahu Fainman. "Demonstration of the DC-Kerr effect in silicon-rich nitride." Optics Letters 46, no. 17 (2021): 4236-4239.

14. Nejadriahi, Hani, Alex Friedman, Rajat Sharma, Steve Pappert, Yeshaiahu Fainman, and Paul Yu. "Thermo-optic properties of silicon-rich silicon nitride for on-chip applications." Optics Express 28, no. 17 (2020): 24951-24960.

15. Lin, Hung-Hsi, Rajat Sharma, Alex Friedman, Benjamin M. Cromey, Felipe Vallini, Matthew W. Puckett, Khanh Kieu, and Yeshaiahu Fainman. "On the observation of dispersion in tunable second-order nonlinearities of silicon-rich nitride thin films." APL Photonics 4, no. 3 (2019): 036101.

16. Puckett, Matthew W., Rajat Sharma, Hung-Hsi Lin, Mu-han Yang, Felipe Vallini, and Yeshaiahu Fainman. "Observation of second-harmonic generation in silicon nitride waveguides through bulk nonlinearities." Optics Express 24, no. 15 (2016): 16923-16933.

17. Tan, D. T. H., K. J. A. Ooi, and D. K. T. Ng. "Nonlinear optics on silicon-rich nitride—a high nonlinear figure of merit CMOS platform." Photonics Research 6.5 (2018): B50-B66.

18. Sohn, Byoung-Uk, Ju Won Choi, Doris KT Ng, and Dawn TH Tan. "Optical nonlinearities in ultra-silicon-rich nitride characterized using z-scan measurements." Scientific reports 9, no. 1 (2019): 1-7.

19. Ooi, K. J. A., D. K. T. Ng, T. Wang, A. K. L. Chee, S. K. Ng, Q. Wang, L. K. Ang, A. M. Agarwal, L. C. Kimerling, and D. T. H. Tan. "Pushing the limits of CMOS optical parametric amplifiers with USRN: Si7N3 above the two-photon absorption edge." Nature communications 8, no. 1 (2017): 1-10.

20. Krückel, Clemens J., Attila Fülöp, Zhichao Ye, and Peter A. Andrekson. "Optical bandgap engineering in nonlinear silicon nitride waveguides." Optics express 25, no. 13 (2017): 15370-15380.

21. Ng, Doris KT, Hongwei Gao, Peng Xing, George FR Chen, Xavier X. Chia, Yanmei Cao, Kenny YK Ong, and Dawn TH Tan. "Enhanced photonics devices based on low temperature plasma-deposited dichlorosilane-based ultra-silicon-rich nitride (Si8N)." Scientific Reports 12, no. 1 (2022): 1-13.

22. Lacava, Cosimo, Stevan Stankovic, Ali Z. Khokhar, T. Dominguez Bucio, F. Y. Gardes, Graham T. Reed, David J. Richardson, and Periklis Petropoulos. "Si-rich silicon nitride for nonlinear signal processing applications." Scientific reports 7, no. 1 (2017): 1-13.

23. Nikitin, Andrey A., Alexandr V. Kondrashov, Vitalii V. Vitko, Ilya A. Ryabcev, Galina A. Zaretskaya, Nikolay A. Cheplagin, Dmitry A. Konkin et al. "Carrier-induced optical bistability in the silicon micro-ring resonators under continuous wave pumping." Optics Communications 480 (2021): 126456.

24. Sharma, Rajat, Matthew W. Puckett, Hung-Hsi Lin, Andrei Isichenko, Felipe Vallini, and Yeshaiahu Fainman. "Effect of dielectric claddings on the electro-optic behavior of silicon waveguides." Optics letters 41, no. 6 (2016): 1185-1188.

25. Bogaerts, Wim, Peter De Heyn, Thomas Van Vaerenbergh, Katrien De Vos, Shankar Kumar Selvaraja, Tom Claes, Pieter Dumon, Peter Bienstman, Dries Van Thourhout, and Roel Baets. "Silicon microring resonators." Laser & Photonics Reviews 6, no. 1 (2012): 47-73.

26. Xing, Peng, Danhao Ma, Lionel C. Kimerling, Anuradha M. Agarwal, and Dawn TH Tan. "High efficiency four wave mixing and optical bistability in amorphous silicon carbide ring resonators." APL Photonics 5, no. 7 (2020): 076110.

27. Grieco, Andrew, Boris Slutsky, Dawn TH Tan, Steve Zamek, Maziar P. Nezhad, and Yeshaiahu Fainman. "Optical bistability in a silicon waveguide distributed Bragg reflector Fabry–Perot resonator." Journal of lightwave technology 30, no. 14 (2012): 2352-2355.

28. Zhang, Ziyang, Matteo Dainese, Marek Chacinski, Lech Wosinski, and Min Qiu. "High-quality-factor micro-ring resonator in amorphous-silicon on insulator structure." (2008): 329-332.

29. Daniel, Brian A., and Govind P. Agrawal. "Phase-switched all-optical flip-flops using two-input bistable resonators." Ieee Photonics Technology Letters 24.6 (2011): 479-481.

30. Yanik, Mehmet Fatih, Shanhui Fan, and Marin Soljačić. "High-contrast all-optical bistable switching in photonic crystal microcavities." Applied Physics Letters 83.14 (2003): 2739-2741.

31. Yoshiki, Wataru, and Takasumi Tanabe. "Analysis of bistable memory in silica toroid microcavity." JOSA B 29.12 (2012): 3335-3343.

Chapter 3

1. Wooten, Ed L., Karl M. Kissa, Alfredo Yi-Yan, Edmond J. Murphy, Donald A. Lafaw, Peter F. Hallemeier, David Maack et al. "A review of lithium niobate modulators for fiber-optic communications systems." IEEE Journal of selected topics in Quantum Electronics 6, no. 1 (2000): 69-82.

2. Janner, Davide, Domenico Tulli, Miguel García-Granda, Michele Belmonte, and Valerio Pruneri. "Micro-structured integrated electro-optic LiNbO3 modulators." Laser & Photonics Reviews 3, no. 3 (2009): 301-313.

3. Wang, Cheng, Mian Zhang, Brian Stern, Michal Lipson, and Marko Lončar. "Nanophotonic lithium niobate electro-optic modulators." Optics express 26, no. 2 (2018): 1547-1555.
4. Sun, Shihao, Mingbo He, Mengyue Xu, Shengqian Gao, Siyuan Yu, and Xinlun Cai. "Hybrid silicon and lithium niobate modulator." IEEE Journal of Selected Topics in Quantum Electronics 27, no. 3 (2020): 1-12.

5. Eltes, Felix, Christian Mai, Daniele Caimi, Marcel Kroh, Youri Popoff, Georg Winzer, Despoina Petousi et al. "A BaTiO 3-based electro-optic Pockels modulator monolithically integrated on an advanced silicon photonics platform." Journal of Lightwave Technology 37, no. 5 (2019): 1456-1462.

6. Petousi, Despoina, Lars Zimmermann, Andrzej Gajda, Marcel Kroh, Karsten Voigt, Georg Winzer, Bernd Tillack, and Klaus Petermann. "Analysis of optical and electrical tradeoffs of traveling-wave depletion-type Si Mach–Zehnder modulators for high-speed operation." IEEE Journal of Selected Topics in Quantum Electronics 21, no. 4 (2014): 199-206.

7. Friedman, Alex, Hani Nejadriahi, Rajat Sharma, and Yeshaiahu Fainman. "Demonstration of the DC-Kerr effect in silicon-rich nitride." Optics Letters 46, no. 17 (2021): 4236-4239.

8. Lin, Hung-Hsi, Rajat Sharma, Alex Friedman, Benjamin M. Cromey, Felipe Vallini, Matthew W. Puckett, Khanh Kieu, and Yeshaiahu Fainman. "On the observation of dispersion in tunable second-order nonlinearities of silicon-rich nitride thin films." APL Photonics 4, no. 3 (2019): 036101.

9. Tan, Dawn TH, D. K. T. Ng, J. W. Choi, E. Sahin, B- U. Sohn, G. F. R. Chen, P. Xing, H. Gao, and Y. Cao. "Nonlinear optics in ultra-silicon-rich nitride devices: recent developments and future outlook." Advances in Physics: X 6, no. 1 (2021): 1905544.

10. Nejadriahi, Hani, Alex Friedman, Rajat Sharma, Steve Pappert, Yeshaiahu Fainman, and Paul Yu. "Thermo-optic properties of silicon-rich silicon nitride for on-chip applications." Optics Express 28, no. 17 (2020): 24951-24960.

11. Ooi, K. J. A., D. K. T. Ng, T. Wang, A. K. L. Chee, S. K. Ng, Q. Wang, L. K. Ang, A. M. Agarwal, L. C. Kimerling, and D. T. H. Tan. "Pushing the limits of CMOS optical parametric amplifiers with USRN: Si7N3 above the two-photon absorption edge." Nature communications 8, no. 1 (2017): 1-10.

12. Lacava, Cosimo, Stevan Stankovic, Ali Z. Khokhar, T. Dominguez Bucio, F. Y. Gardes, Graham T. Reed, David J. Richardson, and Periklis Petropoulos. "Si-rich silicon nitride for nonlinear signal processing applications." Scientific reports 7, no. 1 (2017): 1-13.
13. Sharipov, Ruslan. "Quick introduction to tensor analysis." arXiv preprint math/0403252 (2004).

14. Alloatti, Luca, Clemens Kieninger, Andreas Froelich, Matthias Lauermann, Tobias Frenzel, Kira Köhnle, Wolfgang Freude, Juerg Leuthold, Martin Wegener, and Christian Koos. "Second-order nonlinear optical metamaterials: ABC-type nanolaminates." Applied Physics Letters 107, no. 12 (2015): 121903.

15. Kawamura, Ibuki, Kenji Imakita, Akihiro Kitao, and Minoru Fujii. "Second-order nonlinear optical behavior of amorphous SiOx thin films grown by sputtering." Journal of Physics D: Applied Physics 48, no. 39 (2015): 395101.

16. Levy, Jacob S., Mark A. Foster, Alexander L. Gaeta, and Michal Lipson. "Harmonic generation in silicon nitride ring resonators." Optics express 19, no. 12 (2011): 11415-11421.
17. R. W. Boyd, Nonlinear Optics Third Ed., Elsevier (2003).

18. Isaienko, Oleksandr, and István Robel. "Phonon-assisted nonlinear optical processes in ultrashort-pulse pumped optical parametric amplifiers." Scientific reports 6, no. 1 (2016): 1-12.

19. Ye, Zhichao, Attila Fülöp, Óskar Bjarki Helgason, and Peter A. Andrekson. "Low-loss high-Q silicon-rich silicon nitride microresonators for Kerr nonlinear optics." Optics Letters 44, no. 13 (2019): 3326-3329.

20. Rahman, Hamood Ur, Angus Gentle, Eric Gauja, and Rodica Ramer. "Characterisation of dielectric properties of PECVD Silicon Nitride for RF MEMS applications." In 2008 IEEE International Multitopic Conference, pp. 91-96. IEEE, 2008.

21. Vogt, K. W., M. Houston, M. F. Ceiler, C. E. Roberts, and P. A. Kohl. "Improvement in dielectric properties of low temperature PECVD silicon dioxide by reaction with hydrazine." Journal of electronic materials 24, no. 6 (1995): 751-755.

22. Ceiler, M. F., P. A. Kohl, and S. A. Bidstrup. "Plasma-enhanced chemical vapor deposition of silicon dioxide deposited at low temperatures." Journal of the Electrochemical Society 142, no. 6 (1995): 2067.

23. Tan, D. T. H., K. J. A. Ooi, and D. K. T. Ng. "Nonlinear optics on silicon-rich nitride—a high nonlinear figure of merit CMOS platform." Photonics Research 6.5 (2018): B50-B66.

24. Bogaerts, Wim, Peter De Heyn, Thomas Van Vaerenbergh, Katrien De Vos, Shankar Kumar Selvaraja, Tom Claes, Pieter Dumon, Peter Bienstman, Dries Van Thourhout, and Roel Baets. "Silicon microring resonators." Laser & Photonics Reviews 6, no. 1 (2012): 47-73.

25. Sharma, Rajat, Matthew W. Puckett, Hung-Hsi Lin, Andrei Isichenko, Felipe Vallini, and Yeshaiahu Fainman. "Effect of dielectric claddings on the electro-optic behavior of silicon waveguides." Optics letters 41, no. 6 (2016): 1185-1188.

26. Zhang, Ziyang, Matteo Dainese, Marek Chacinski, Lech Wosinski, and Min Qiu. "High-quality-factor micro-ring resonator in amorphous-silicon on insulator structure." (2008): 329-332.

27. Xiao, Shijun, Maroof H. Khan, Hao Shen, and Minghao Qi. "Modeling and measurement of losses in silicon-on-insulator resonators and bends." Optics Express 15, no. 17 (2007): 10553-10561.